# A 4D Hyperspherical Interpretation of *q*-Space

**A. Pasha Hosseinbor**[a,*], **Moo K. Chung**[a,b], **Yu-Chien Wu**[c], **Barbara B. Bendlin**[d], and **Andrew L. Alexander**[a,e,f]

[a]Waisman Laboratory for Brain Imaging and Behavior, University of Wisconsin-Madison, Madison, WI, USA

[b]Department of Biostatistics and Medical Informatics, University of Wisconsin-Madison, Madison, WI USA

[c]Center for Neuroimaging, Indiana University, Indianapolis, IN, USA

[d]Geriatric Research, Education and Clinical Center (GRECC), William S. Middleton Memorial Veteran's Hospital, University of Wisconsin-Madison, Madison, WI, USA

[e]Department of Medical Physics, University of Wisconsin-Madison, Madison, WI, USA

[f]Department of Psychiatry, University of Wisconsin-Madison, Madison, WI, USA

## Abstract

3D *q*-space can be viewed as the surface of a 4D hypersphere. In this paper, we seek to develop a 4D hyperspherical interpretation of *q*-space by projecting it onto a hypersphere and subsequently modeling the *q*-space signal via 4D hyperspherical harmonics (HSH). Using this orthonormal basis, we derive several well-established *q*-space indices and numerically estimate the diffusion orientation distribution function (dODF). We also derive the integral transform describing the relationship between the diffusion signal and propagator on a hypersphere. Most importantly, we will demonstrate that for hybrid diffusion imaging (HYDI) acquisitions low order linear expansion of the HSH basis is sufficient to characterize diffusion in neural tissue. In fact, the HSH basis achieves comparable signal and better dODF reconstructions than other well-established methods, such as Bessel Fourier orientation reconstruction (BFOR), using fewer fitting parameters. All in all, this work provides a new way of looking at *q*-space.

## Keywords

Hyperspherical Harmonics; Diffusion Propagator; ODF; *q*-Space Indices; Diffusion MRI

*Corresponding author: hosseinbor@wisc.edu, A. Pasha Hosseinbor.

## 1. Introduction

The aim of diffusion magnetic resonance imaging (dMRI) is to non-invasively recover information about the diffusion of water molecules in biological tissues. An important mathematical descriptor of the water diffusion profile is the ensemble average propagator (EAP), which is a probability density function that describes the (canonically averaged) likelihood of a water molecule undergoing a net displacement during the diffusion time. The EAP can characterize complex neural architecture, such as crossing fibers, and many quantitative features of the water diffusion profile can be derived from the EAP.

Under the narrow pulse assumption (Stejskal and Tanner, 1965), the measured MR signal attenuation, $E(\mathbf{q})$, in $q$-space and the EAP, $P(\mathbf{k})$, are Fourier Transform pairs (Callaghan, 1991):

$$P(\mathbf{k}) = \int E(\mathbf{q}) e^{-2\pi i \mathbf{q} \cdot \mathbf{k}} d^3 \mathbf{q}, \quad (1)$$

where $\mathbf{k}$ is the displacement vector in EAP-space and $\mathbf{q}$ is the diffusion wave-vector in signal-space. We denote $\mathbf{q} = q\mathbf{u}(\theta, \varphi)$ and $\mathbf{k} = k\mathbf{r}(\theta', \varphi')$, where $\mathbf{u}$ and $\mathbf{r}$ are 3D unit vectors. The wave vector $\mathbf{q}$ is $\mathbf{q} = \gamma \delta \mathbf{G}/2\pi$, where $\gamma$ is the nuclear gyromagnetic ratio and $\mathbf{G} = g\mathbf{u}$ is the applied diffusion gradient direction. The norm of the wave vector, $q$, is related to the diffusion weighting level ($b$-value) via $b = 4\pi^2 q^2(\ - \delta/3)$ (Basser, 2002), where $\delta$ is the duration of the applied diffusion gradients and the time between the two pulses. Eq. (1) is valid only if the narrow pulse condition is met, which is rarely the case for $q$-space dMRI performed under experimental conditions. Several studies (Mair et al., 2002; Weeden et al., 2005; Bar-Shir et al., 2008) however, have shown that even when these assumptions do not hold, the Fourier relationship in Eq. (1) is still a reasonable approximation of the microstructural features. The diffusion displacements, however, will be consistently underestimated (Weeden et al., 2005).

Another mathematical descriptor of the water diffusion profile is the diffusion orientation distribution function (dODF), which is simply an angular feature of the EAP The dODF, denoted as $\psi$, is defined as the radial projection of the EAP on the unit sphere (Canales-Rodriguez et al., 2010):

$$\psi_\kappa(\mathbf{r}) = \frac{1}{O_\kappa} \int_0^\infty P(k, \mathbf{r}) k^\kappa dk, \quad (2)$$

where $\kappa$ is the order of the radial projection and $O_\kappa$ is the normalization constant. The dODF is thus the (angular) marginal density function of the EAP that describes the likelihood of a water molecule diffusing into any given solid angle $\mathbf{r}$ during the diffusion time. The classical dODF was introduced by (Tuch, 2004) as the zeroth-order radial projection, i.e. $\psi_0(\mathbf{r})$.

Many dMRI methods already exist that seek to estimate the EAP and dODF. The most widely used dMRI technique, diffusion tensor imaging (DTI) (Basser et al., 1994), assumes the EAP is described by a multivariate Gaussian function. However, DTI's inherent assumption of Gaussianity is an over-simplification of water diffusion in the brain, and so voxels containing complex neural architecture (e.g. crossing fibers) can not be properly

described by DTI. In order to recover complex white matter (WM) geometry, high angular resolution diffusion imaging (HARDI) (Tuch et al., 2002) was proposed, and many HARDI techniques can be used to measure the dODF (Tuch, 2004; Hess et al., 2006; Descoteaux et al., 2007; Canales-Rodriguez et al., 2009; Tristan-Vega et al., 2009; Aganj et al., 2010; Michailovich et al., 2011). HARDI, in general, does not sample all of $q$-space but rather confines the signal measurements to a single spherical shell in $q$-space (i.e. single $b$-value). Since the dODF is defined as the radial projection of the EAP, whose estimation requires measurements across all of $q$-space, HARDI gives an incomplete picture of the dODF. Diffusion spectrum imaging (DSI) (Weeden et al., 2005) and hybrid diffusion imaging (HYDI) (Wu and Alexander, 2007) are multiple $b$-value techniques that estimate the EAP directly from the raw $q$-space data by evaluating Eq. (1) using the Fast Fourier Transform (FFT). The difference between the two methods lies in their sampling schemes: DSI directly samples the $q$-space signal on a Cartesian lattice whereas HYDI samples it along concentric spherical shells. DSI requires dense sampling of the lattice (~ 500 diffusion measurements), which means long acquisition times and very strong diffusion gradients. HYDI uses much fewer samples than DSI (~ 125), but it requires the spherical measurements to be interpolated and regridded onto a Cartesian lattice to perform the FFT, and such *ad hoc* processing may have adverse effects on HYDI's EAP estimation.

In recent years, non-parametric modeling of the $q$-space signal $E(\mathbf{q})$, in terms of either an orthonormal or non-orthonormal basis, has become popular among multiple $b$-value methods because it can facilitate the obtainment of closed-form solutions of the EAP and dODF and/or sparse representation of the diffusion process. Each of these non-parametric EAP methods offers its own unique interpretation of $q$-space, which revolves around the basis chosen to describe $E(\mathbf{q})$. Prominent non-parametric EAP methods include diffusion propagator imaging (DPI) (Descoteaux et al., 2011), simple harmonic oscillator based reconstruction and estimation (SHORE) (Ozarslan et al., 2008, 2009), spherical polar Fourier imaging (SPFI) (Assemlal et al., 2009a; Cheng et al., 2010a, b), Bessel Fourier orientation reconstruction (Hosseinbor et al., 2013a), sparse multi-shell diffusion imaging (SMDI) (Rathi et al., 2011), and mean apparent propagator (MAP) MRI (Ozarslan et al., 2013). These methods are summarized in Table 1.

Each of the methods described in Table 1, naturally, confines their analysis to 3D. But just as a circle may be viewed as a cross-section of a sphere, 3D $q$-space may be viewed as a cross-section of a 4D hypervolume. Specifically, 3D $q$-space may be embedded onto the surface of a 4D hypersphere via stereographic projection, and so 3D $q$-space can be regarded as constituting a single hypersphere in 4D space. An interesting question is then what insights will be revealed by a higher-dimensional analysis of 3D $q$-space.

Although it may seem counterintuitive, higher-dimensional analysis of a 3D problem can prove to be surprisingly useful, as is illustrated by the case of the hydrogen atom. One of the first physical applications of quantum mechanics was in solving the Schrödinger equation for the hydrogen atom. It had been solved in position-space by Schrödinger, himself (Schrödinger, 1926), but not in momentum-space, which is related to position-space via the Fourier transform. The momentum-space solution was of interest to quantum chemists because it could potentially reveal additional quantum mechanical insights about the

hydrogen atom not found in the position space solution. Nearly a decade after Schrödinger's landmark publication, V. Fock solved the Schrödinger equation for the hydrogen atom directly in momentum-space. In his classic paper (Fock, 1935), Fock stereographically projected 3D momentum-space onto the surface of a 4D unit hypersphere, and after this mapping was made, he was able to show that the momentum-space hydrogen orbitals could be simply expressed in terms of 4D hyperspherical harmonics (HSH), which are the multidimensional analogues of the 3D spherical harmonics.

In this paper, we seek to develop a 4D hyperspherical interpretation of $q$-space (Hosseinbor et al., 2013b). Following the work of Fock, we model the 3D $q$-space signal in terms of the 4D HSH, which is achieved by stereographically projecting 3D $q$-space onto the surface of a 4D hypersphere. Employing a hybrid, non-Cartesian encoding scheme, we estimate the dODF using the HSH framework and BFOR and assess their performances. We also compute familiar $q$-space metrics such as zero-displacement probability (*Po*) (Assaf et al., 2000; Wu and Alexander, 2007) and $q$-space inverse variance (QIV) (Wu et al., 2008; Hosseinbor et al., 2013a). Most importantly, we will show that such high-dimensional analysis of $q$-space allows for sparser representation of the diffusion process than BFOR.

The paper is organized as follows: in **Section 2**, we review the 4D HSH and stereographic projection, derive the relationship between the $q$-space signal and EAP on the hypersphere, and discuss how to estimate the dODF and several $q$-space indices using the HSH basis. In **Section 3**, we describe the numerical implementation details of the HSH-framework and present the synthetic and *in vivo* human brain datasets that will be used to validate it and compare it BFOR in **Section 4**. A discussion then ensues in **Section 5**.

## 2. Theory

### 2.1. 4D Hyperspherical Harmonics

Consider the 4D unit hypersphere $S^3$ existing in $\mathbb{R}^4$. The Laplace-Beltrami operator on $S^3$ is defined as,

$$\Delta_{S^3} = \frac{1}{\sin^2\beta} \frac{\partial}{\partial\beta} \sin^2\beta \frac{\partial}{\partial\beta} + \frac{1}{\sin^2\beta} \Delta_{S^2}$$

where $\Delta_{S^2}$ is the Laplace-Beltrami operator on the unit sphere $S^2$. The eigenfuctions of $\Delta_{S^3}$ are the 4D HSH $Z_{nl}^m(\beta, \theta, \phi)$:

$$\Delta_{S^3} Z_{nl}^m = -l(l+2) Z_{nl}^m$$

The 4D HSH are defined as (Domokos, 1967)

$$Z_{nl}^m(\beta, \theta, \phi) = 2^{l+1/2} \sqrt{\frac{(n+1)\Gamma(n-l+1)}{\pi\Gamma(n+l+2)}} \Gamma(l+1) \sin^l\beta \, G_{n-l}^{l+1}(\cos\beta) \, Y_l^m(\theta, \phi), \quad (3)$$

where $(\beta, \theta, \varphi)$ obey $(\beta \in [0, \pi], \theta \in [0, \pi], \varphi \in [0, 2\pi])$, $G_{n-1}^{l+1}$ are the Gegenbauer (ultraspherical) polynomials, and $Y_l^m$ are the 3D spherical harmonics. The Gegenbauer polynomials can be expressed in terms of the Gaussian (ordinary) hyper geometric function:

$$G_\alpha^\lambda(x) = \frac{\Gamma(\alpha+2\lambda)}{\alpha!\Gamma(2\lambda)} \, {}_2F_1\left(-\alpha, \alpha+2\lambda; \lambda+\frac{1}{2}; \frac{1}{2}(1-x)\right)$$

The integers $l$ and $m$ denote the degree and order of the HSH, respectively, and $n = 0, 1, 2,$ …. These three integers obey the conditions $0 \le l \le n$ and $-l \le m \le l$. The number of HSH corresponding to a given value of $n$ is $(n + 1)^2$. The first few 4D HSH are shown in Table 2. The HSH form an orthonormal basis on the hypersphere, and the normalization condition reads

$$\int_0^{2\pi}\int_0^\pi\int_0^\pi Z_{nl}^m(\beta,\theta,\phi)Z_{n'l'}^{m'\,*}(\beta,\theta,\phi)\sin^2\beta\sin\theta d\beta d\theta d\phi = \delta_{nn'}\delta_{ll'}\delta_{mm'} \quad (4)$$

## 2.2. 4D Stereographic Projection of q-Space onto Hypersphere

For centuries, cartographers have struggled with the problem of how to represent the spherical-like surface of the Earth on a flat sheet of paper. One way to achieve this is via stereographic projection. To illustrate it, consider the simpler 3D case. The goal of stereographic projection is to associate each 2D point $(u, v)$ in the equatorial plane with a unique point $P = (x, y, z)$ on the unit sphere. To achieve this, we construct the 3D line that passes through the north pole $N = (0, 0, 1)$ of the sphere and the given point $(u, v, 0)$. This line touches the surface of the sphere at exactly one point, $P$, and so the point $P = (x, y, z)$ is the stereographic projection of the point $(u, v)$.

In order to model the $q$-space signal with the HSH, we need to map 3D $q$-space onto a 4D hypersphere of radius $r_o$, which can be achieved via stereographic projection. The $q$-space coordinates are defined as

$$q_x = q\sin\theta\cos\phi \quad q_y = q\sin\theta\sin\phi \quad q_z = q\cos\theta$$

The coordinates of the signal-hypersphere are defined by the 4D vector $\mathbf{s}$, whose components are

$$s_1 = r_o\sin\beta\sin\theta\cos\phi$$
$$s_2 = r_o\sin\beta\sin\theta\sin\phi$$
$$s_3 = r_o\sin\beta\cos\theta$$
$$s_4 = r_o\cos\beta.$$

Please note that the hypersphere radius $r_o$ has the same dimension as $q$. We will now derive the relationship between $\mathbf{q}$ and $\mathbf{s}$ as given by stereographic projection.

The 4D line that passes through the north pole of the hypersphere, $(0, 0, 0, r_o)$, and some point in $q$-space $(q_x, q_y, q_z)$ is parameterized as

$$s_1 = tq_x, \quad s_2 = tq_y, \quad s_3 = tq_z, \quad s_4 = r_o(1-t), \quad -\infty < t < \infty \quad (5)$$

The line touches the hypersphere when $t$ satisfies

$$r_o^2 = s_1^2 + s_2^2 + s_3^2 + s_4^2 = t^2(q_x^2 + q_y^2 + q_z^2) + r_o^2(1 - 2t + t^2), \quad (6)$$

whose solution is $t = 2r_o^2/(q^2 + r_o^2)$. Substituting our solution back into Eq. (5) gives the relationship between the two coordinate spaces:

$$\begin{aligned}
s_1 &= \frac{2r_o^2 q_x}{q^2 + r_o^2} = r_o \sin\beta \sin\theta \cos\phi \\
s_2 &= \frac{2r_o^2 q_y}{q^2 + r_o^2} = r_o \sin\beta \sin\theta \sin\phi \\
s_3 &= \frac{2r_o^2 q_z}{q^2 + r_o^2} = r_o \sin\beta \cos\theta \\
s_4 &= \frac{r_o(q^2 - r_o^2)}{q^2 + r_o^2} = r_o \cos\beta
\end{aligned} \quad (7)$$

According to Eq. (7), the center of $q$-space $(0, 0, 0)$ projects onto the south pole $(0, 0, 0, -r_o)$ of the hypersphere. As $q \to \infty$, the projection $(s_1, s_2, s_3, s_4)$ moves closer to the north pole $(0, 0, 0, r_o)$. Eq. (7) establishes a one-to-one correspondence between $q$-space and the 4D hypersphere. The radius of the hypersphere $r_o$ controls the density of the projected $q$-space points onto the surface of the hypersphere.

Stereographic projection exhibits two important properties. First, it is conformal, which means it preserves angles - the angles $(\theta, \varphi)$ in $q$-space are preserved in 4D hyperspherical space. However, stereographic projection does not preserve volume; in general, the volume of a region in the 3D plane doesn't equal the volume of its projection onto the hypersphere. In fact, the degree of volume distortion in going from a differential volume element in $q$-space $d^3\mathbf{q}$ to that of the hypersphere $dV = r_o^3 d\Omega$ can be shown to be

$$d^3\mathbf{q} = \left(\frac{q^2 + r_o^2}{2r_o}\right)^3 \frac{1}{r_o^3} dV = \left(\frac{q^2 + r_o^2}{2r_o}\right)^3 d\Omega = \left(\frac{r_o}{1 - \cos\beta}\right)^3 d\Omega, \quad (8)$$

where $d\Omega = \sin^2\beta \sin\theta d\beta d\theta d\varphi$ is the differential area of the hypersphere. We will derive Eq. (8) in **Section 2.4**.

## 2.3. Diffusion Signal Modeling via HSH Basis

Stereographically projecting $q$-space onto the hypersphere results in the $q$-space signal existing along the surface of the hypersphere. According to Fourier analysis, any square-integrable function defined on a sphere can be expanded in terms of the spherical harmonics. Thus, stereographic projection allows the 3D $q$-space signal to be expanded in terms of the HSH:

$$E_{r_o}(\beta, \theta, \phi) \approx \sum_{n=0}^{N} \sum_{l=0}^{n} \sum_{m=-l}^{l} C_{nlm} Z_{nl}^{m}(\beta, \theta, \phi), \quad (9)$$

where $E_{r_o}$ denotes the $q$-space signal existing on hypersphere of radius $r_o$ and $C_{nlm}$ are the HSH expansion coefficients. The realness of the diffusion signal requires use of the real HSH, and so we employ a modified real basis proposed in (Koay et al., 2009) for $Y_l^m$.

An important axiom to state is that the $q$-space signal, itself, remains invariant after the mapping - that is, for a given $q$-space point $(q_x, q_y, q_z)$ and its corresponding projection on the hypersphere $(s_1, s_2, s_3, S_4)$, $E(q_x, q_y, q_z) = E_{ro}(s_1, s_2, s_3, S_4)$. In $q$-space, the diffusion signal is even i.e. $E(q_x, q_y, q_z) = E(-q_x, -q_y, -q_z)$. Evenness in $q$-space doesn't necessarily translate into evenness on the hypersphere. According to Eq. (7), $(-q_x, -q_y, -q_z)$ projects to $(-S_1, -S_2, -S_3, S_4)$, and so evenness in $q$-space is tantamount to

$$E_{r_o}(s_1, s_2, s_3, s_4) = E_{r_o}(-s_1, -s_2, -s_3, s_4)$$

on the hypersphere, indicating that the signal is not even on the hypersphere. In other words, stereographic projection destroys evenness, i.e. a function even in the plane is no longer even on the sphere upon projection. For this reason, we are free to use both the even and odd HSH. Thus, for a given truncation order $N$, the total number of expansion coefficients is

$$W = (N+1)(N+2)(2N+3)/6$$

## 2.4. Relationship between EAP and q-Space Signal on Hypersphere

Since our analysis of 3D $q$-space is confined to the hypersphere, a natural course of action would be to stereographically project 3D EAP-space onto its own hypersphere. But the Fourier relationship given in Eq. (1) between the signal attenuation and EAP does not hold true on the hypersphere. The question, then, is what integral transform maps from the signal-hypersphere to the EAP-hypersphere, and this problem is illustrated in Fig. 1. Phrasing the problem more generally, we seek the integral transform that describes the relationship between any two functions individually existing on some $n$-dimensional sphere $S^n$, given that the two functions are Fourier Transform pairs on the $(n-1)$-plane. We will now proceed to derive this hyperspherical integral transform, which has never been derived before.

Any point in 3D EAP space, the Fourier pair of $q$-space, is given by

$$k_x = k\sin\theta'\cos\phi' \quad k_y = k\sin\theta'\sin\phi' \quad k_z = k\cos\theta'$$

Now lets stereographically project 3D EAP-space onto a 4D hypersphere of radius $r_o$, whose coordinates are defined by the 4D vector $\mathbf{v} = (v_1, v_2, v_3, v_4)$. The relationship between $\mathbf{k}$ and $\mathbf{v}$ is then

$$
\begin{aligned}
v_1 &= \frac{2r_o^2 k_x}{k^2 + r_o^2} = r_o \sin\beta' \sin\theta' \cos\phi' \\
v_2 &= \frac{2r_o^2 k_y}{k^2 + r_o^2} = r_o \sin\beta' \sin\theta' \sin\phi' \\
v_3 &= \frac{2r_o^2 k_z}{k^2 + r_o^2} = r_o \sin\beta' \cos\theta' \\
v_4 &= \frac{r_o(k^2 - r_o^2)}{k^2 + r_o^2} = r_o \cos\beta'
\end{aligned}
\tag{10}
$$

Lets now express the Fourier kernel in Eq. (1) in terms of the hyperspherical coordinates displayed in (7) and (10). The dot product of the 3D vectors $\mathbf{q}$ and $\mathbf{k}$ is

$$
\mathbf{q} \cdot \mathbf{k} = qk[\sin\theta\cos\phi\sin\theta'\cos\phi' + \sin\theta\sin\phi\sin\theta'\sin\phi' + \cos\theta\cos\theta'] \tag{11}
$$

Similarly, the dot project of the 4D vectors $\mathbf{s}$ and $\mathbf{v}$ is

$$
\frac{\mathbf{s} \cdot \mathbf{v}}{r_o^2 \sin\beta\sin\beta'} = \sin\theta\cos\phi\sin\theta'\cos\phi' + \sin\theta\sin\phi\sin\theta'\sin\phi' + \cos\theta\cos\theta' + \frac{\cos\beta\cos\beta'}{\sin\beta\sin\beta'} \tag{12}
$$

We know from (7) that $\frac{q^2 - r_o^2}{q^2 + r_o^2} = \cos\beta$, which means $q = r_o\sqrt{\frac{1+\cos\beta}{1-\cos\beta}}$. Similarly, $k = r_o\sqrt{\frac{1+\cos\beta'}{1-\cos\beta'}}$. The relationship between the two dot products, (11) and (12), is then

$$
\mathbf{q} \cdot \mathbf{k} = \frac{1}{(1-\cos\beta)(1-\cos\beta')}(\mathbf{s} \cdot \mathbf{v} - s_4 v_4) \tag{13}
$$

The next and final step is to find the relationship between the differential volume element in $q$-space, $d^3\mathbf{q}$, and that of the hypersphere, $dV$. The differential volume element in $q$-space is simply $d^3\mathbf{q} = q^2 \sin\theta dq d\theta d\varphi$, while that of the hyperpshere is $dV = r_o^3 \sin^2\beta \sin\theta d\beta d\theta d\phi$.

Since $\cos\beta = \frac{q^2 - r_o^2}{q^2 + r_o^2}$, it can be shown then that $\frac{d\beta}{dq} = \frac{2r_o}{q^2 + r_o^2}$ and $\sin^2\beta = \left(\frac{2r_o q}{q^2 + r_o^2}\right)^2$. Hence, we have

$$
d^3\mathbf{q} = \left(\frac{q^2 + r_o^2}{2r_o}\right)^3 d\Omega = \left(\frac{r_o}{1-\cos\beta}\right)^3 d\Omega,
$$

which is simply Eq. (8).

Substituting relations (13) and (8) into Eq. (1) gives the integral transform relating the signal-hypersphere to that of the EAP:

$$
P_{r_o}(\mathbf{v}) = r_o^3 \int E_{r_o}(\mathbf{s}) \frac{e^{-2\pi i[\mathbf{s}\cdot\mathbf{v} - s_4 v_4]/(1-\cos\beta)(1-\cos\beta')}}{(1-\cos\beta)^3} d\Omega, \tag{14}
$$

where $P_{r_o}$ denotes the EAP existing on hypersphere of radius $r_o$. Just as with the $q$-space signal, the EAP remains invariant after the mapping. Eq. (14) is not one of the more familiar integral transforms encountered in mathematics literature.

## 2.5. HSH Metrics

A well-known $q$-space metric is $Po \equiv P(\mathbf{k} = 0)$ (Assaf et al., 2000; Wu and Alexander, 2007), which is a measure of how minimally diffusive a water molecule is during the diffusion time. The origin $\mathbf{k} = 0$ in 3D EAP-space corresponds to the south pole of the EAP-hypersphere i.e. $\beta' = \pi$. Hence using Eq. (14) and the HSH basis, we can derive $Po$ on the hypersphere:

$$Po = P_{r_o}(\beta' = \pi) = \int_{\Omega \in S^3} \frac{E_{r_o}(\mathbf{s})}{(1 - \cos\beta)^3} d\Omega = \int_{\Omega \in S^3} \left( \frac{q^2 + r_o^2}{2r_o} \right)^3 E_{r_o}(\mathbf{s}) d\Omega \quad (15)$$

The integral in (15) is difficult to evaluate analytically, which is due to the non-volume-preserving nature of stereographic projection; the signal is now weighted by the distortion factor in the integration.

The $q$-space inverse variance (QIV) (Wu et al., 2008; Hosseinbor et al., 2013a) is a measure of the average diffusion displacements from $q$-space measurements, and is an alternative measure of diffusivity to the mean square displacement (MSD). The QIV is a more robust measure of diffusivity than the MSD, especially when high $b$-values are concerned, and exhibits white matter/gray matter contrast unlike the MSD (Hosseinbor et al., 2012). The QIV is defined mathematically as QIV $= [\int q^2 E(q) d^3 q]^{-1}$. Taking into account the volume distortion factor described by Eq. (8) upon stereographic projection of the $q$-space signal, the QIV becomes

$$\text{QIV} = \left[ \int q^2 \left( \frac{q^2 + r_o^2}{2r_o} \right)^3 E_{r_o}(\mathbf{s}) d\Omega \right]^{-1} \quad (16)$$

As with Eq. (15) for $Po$, Eq. (16) is difficult to evaluate analytically due to the weighting of the distortion factor in the integration.

In order to evaluate the integrals in (15) and (16), we will first compute uncorrected versions of $Po$ and QIV by not weighting the distortion factor in the integration. Let $\gamma$ denote some metric of interest that is derived from the integration of the $q$-space signal along the surface of the hypersphere:

$$\Upsilon = \int_{\Omega \in S^3} E_{r_o}(\Omega) dV = r_o^3 \sum_{n,l,m} C_{nlm} \int_{\Omega \in S^3} Z_{nl}^m(\Omega) d\Omega$$
$$= \pi \sqrt{2} r_o^3 C_{000} \quad (17)$$

where we use the fact that $Z_{00}^0 = \frac{1}{\pi\sqrt{2}}$. The QIV and $Po$ can then be obtained from $\gamma$ by numerically performing a signal weighting operation that will correct for the volume distortion, which will be discussed in detail in the **Numerical Implementation** section.

### 2.6. Estimation of dODF

Given the intricacy of Eq. (14), it is difficult to estimate the EAP analytically using the HSH framework. However, the classical dODF $\psi_0(\mathbf{r})$ can be numerically estimated from the signal measurements using the FFT. Lets construct a $11 \times 11 \times 11$ ($-q_{max} : q : q_{max}$) Cartesian lattice, which we map onto the 4D hypersphere via Eq. (7). Once we have computed the HSH expansion coefficients via LLS from the acquired data, Eq. (9) can then be used the estimate the signal at any location on the hypersphere, including the projected lattice points. The stereographic projection establishes a one-to-one correspondence between the lattice and hypersphere, meaning that a given lattice point and its corresponding projection on the hypersphere have the same signal value. Hence, taking the FFT of the HSH-estimated signal for the lattice gives the EAP. The $\kappa = 0$ radial projection of the EAP, as given by Eq. (2), then yields the dODF. Since the zeroth-order dODF is not inherently normalized, we min-max normalize it (Tuch, 2004).

## 3. Materials and Methods

### 3.1. Numerical Implementation

In general, we are given $k$ HARDI shell datasets. The number of encoding directions in each shell does not have to be the same. Each HARDI dataset corresponds to a different $b$-value. Across all $k$ shells, we have total of $M$ diffusion measurements (including the $b = 0$ measurement). The task then is to estimate the coefficients $C_{nlm}$ in Eq. (9) from the observed signal.

Let $\Omega_j = (\beta_j, \theta_j, \varphi_j)$ denote the hyper spherical angles corresponding to the $j^{th}$ diffusion measurement. Denote $\mathbf{G}$ as the $M \times 1$ vector representing the $M$ diffusion signal measurements across all $k$ shells, $\mathbf{C}$ the $W \times 1$ vector of unknown expansion coefficients $C_{nlm}$, and $\mathbf{A}$ the $M$ x $W$ matrix constructed with the HSH basis

$$\mathbf{A} = \begin{pmatrix} Z_{00}^0(\Omega_1) & Z_{10}^0(\Omega_1) & Z_{11}^{-1}(\Omega_1) & Z_{11}^0(\Omega_1) & Z_{11}^1(\Omega_1) & \cdots & Z_{NN}^N(\Omega_1) \\ \vdots & \vdots & \vdots & \vdots & \ddots & \vdots \\ Z_{00}^0(\Omega_M) & Z_{10}^0(\Omega_M) & Z_{11}^{-1}(\Omega_M) & Z_{11}^0(\Omega_M) & Z_{11}^1(\Omega_M) & \cdots & Z_{NN}^N(\Omega_M) \end{pmatrix}$$

Thus, we have a linear model of the form $\mathbf{G} = \mathbf{AC}$. This system of over-determined equations is solved via linear least squares with Laplace-Beltrami regularization (LBR), yielding $\hat{\mathbf{C}} = (\mathbf{A}^T\mathbf{A} + \lambda_l\mathbf{L}_{reg})^{-1}\mathbf{A}^T\mathbf{G}$, where $\mathbf{L}_{reg}$ is the LBR diagonal matrix with entries $l^2(l + 2)^2$ along the diagonal. The regularization serves to reinforce the positivity constraint of the signal.

Comparing Eq. (15) and (17), we see that $Po$ is distorted by a factor given by Eq. (8). We correct for this volume distortion by weighting each signal shell in $q$-space by $\left(\frac{q_i^2 + r_o^2}{2r_o}\right)^3$, where $q_i$ is the radius of the $i^{th}$ shell, before signal fitting. The resulting "weighted" coefficients are then solely used for computing $Po$ via Eq. (17). The $q$-shell radii are listed in

Table 3. Such $q$-shell weighting has been employed in (Wu et al., 2008) in the estimation of *Po*.

Similarly, comparing Eq. (16) and (17), we see that the QIV is distorted by a factor $q^2 \left( \frac{q^2 + r_o^2}{2r_o} \right)^3$. We correct for this volume distortion by weighting each signal shell in $q$-space by $q_i^2 \left( \frac{q_i^2 + r_o^2}{2r_o} \right)^3$ before signal fitting. The resulting "weighted" coefficients are then solely used for computing QIV via Eq. (17).

## 3.2. Interpolation via HSH Basis

Once the coefficients are estimated, the signal attenuation can be evaluated at any location along the hypersphere using Eq. (9). 1000 uniformly distributed vertices on a unit sphere in $q$-space (i.e. 1000 values of $\theta$ and $\varphi$) were acquired using the approach described in (Wong and Roos, 1994), and then stereographically projected onto the hypersphere. The $q$-space signal $E_{r_o}$ ($\beta$, $\theta$, $\varphi$) was then interpolated along these 1000 points.

## 3.3. Diffusion MRI Data Acquisitions for Synthetic and In Vivo Data

The synthetic and *in vivo* datasets use a hybrid, non-Cartesian $q$-space sampling scheme (HYDI) (Wu and Alexander, 2007), shown in Table 3. Since ODF reconstruction is sensitive to angular resolution, the number of encoding directions is increased with each shell to increase the angular resolution with the level of diffusion weighting. The number of directions in the outer shells were increased to better characterize complex tissue architecture.

**3.3.1. Synthetic Data**—At low $b$-values (i.e. $b \sim 1000$ s/mm$^2$), the diffusion signal decay is mono-exponential. However, dMRI experiments using high $b$-values ($> 2000$ s/mm$^2$) have shown that the diffusion signal decay is no longer mono-exponential. Studies in normal human brain, with $b$-values over an extended range of up to 6000 s/mm$^2$, have shown that the signal decay is better described with a bi-exponential curve (Mulkern et al., 1999; Clark and Le Bihan, 2000). Similar findings were made for rat brain, using multiple $b$-values of up to 10000 s/mm$^2$ (Niendorf et al., 1996). And according to (Assaf and Cohen, 1998), a bi-exponential fit gives very good agreement with the observed water signal attenuation in excised brain tissue from rats for $b$-values of up to $2 - 3 \times 10^4$ s/mm$^2$. Therefore, the HSH basis and BFOR were applied to simulations of crossing fiber configurations generated by a bi-exponential mixture model.

In the bi-exponential mixture model,

$$E(q, \mathbf{u}) = \sum_{k=1}^{N_b} [f_{kf} e^{-b\mathbf{u}^T \mathbf{D}_{kf} \mathbf{u}} + f_{ks} e^{-b\mathbf{u}^T \mathbf{D}_{ks} \mathbf{u}}], \quad (18)$$

where $N_b$ is the total number of simulated fibers, $f_{kf}$ the volume fraction of the fast component of the $k^{th}$ fiber, and $f_{ks}$ the volume fraction of the slow component. The summation of all volume fractions is 1, i.e., $\sum_{k=1}^{N_b} [f_{kf} + f_{ks}] = 1$. $D_{kf}$ and $D_{ks}$ describe the

diffusion tensor for the fast and slow components, respectively, of the $k^{th}$ fiber assuming no exchange between the fast- and slow-diffusion compartments. The values of the fast and slow Gaussian diffusion functions were taken from (Maier et al., 2004) and are shown in Table 4. It should be noted that there is controversy over the assignment of these components and whether the bi-exponential model should take into account exchange between compartments (Mulkern et al., 1999).

We look at two equally weighed fibers crossing at 45° and 75°, and set eigenvalues of each diffusion tensor to be [1.6,0.4,0.4]e-3 mm²/s, which gives FA=0.7071. Monte Carlo noise simulations were performed to investigate the effect of SNR on the signal and dODF reconstructions. Five SNR levels ([10 20 30 40 80]) for the $b = 0$ image were simulated, 1000 times each, by adding Rician noise in a similar manner as in (Descoteaux et al., 2007). The HSH estimations are performed using the $N = 2$ ($W = 14$ fitting parameters), 3 ($W = 30$), & 4 ($W = 55$) truncation orders and $\lambda_l = 10^{-6}$. The appropriate hypersphere radius for each truncation order will be discussed in the **Results Section**. BFOR parameters are taken from (Hosseinbor et al., 2013a): the radial and angular truncation orders are chosen to be 6 and 4, respectively, yielding 90 fitting parameters.

We assess the quality of the signal fit by computing the normalized mean squared error (NMSE):

$$\text{NMSE} = \frac{\|S - \hat{S}\|^2}{\|S\|^2},$$

where $S$ is the ground truth signal given by Eq. (18) and $\hat{S}$ is the HSH-estimated signal described by Eq. (9). Similarly, the quality of the dODF reconstruction is assessed by computing the Kullback-Leibler divergence (KLD) and angular error (Tuch, 2004). The KLD is

$$\text{KLD} = \sum_i \ln \left( \frac{\psi(\mathbf{r}_i)}{\hat{\psi}(\mathbf{r}_i)} \right) \psi(\mathbf{r}_i),$$

where $\psi$ and $\hat{\psi}$ are the ground truth and estimated dODFs, respectively. The ground truth dODF was found by taking the FTT of Eq. (18). The angular error metric is defined as

$$\alpha = \arccos|(\hat{\mathbf{r}}^*)^T \mathbf{r}^*|,$$

where $\hat{\mathbf{r}}^* = \arg\max_{\mathbf{r}} \hat{\psi}(\mathbf{r})$ and $\mathbf{r}^* = \arg\max_{\mathbf{r}} \psi(\mathbf{r})$.

**3.3.2. Human Brain Data**—HYDI was performed on a healthy, adult human using a 3 T GE-SIGNA whole body scanner with ASSET parallel imaging. MR parameters were TE=102 ms, TR=6500 ms, FOV=24 cm, matrix=96 × 96, voxel size=2.5 × 2.5 mm², 43

slices with slice thickness=3 mm, and scan time=15 min. Diffusion parameters were gradient duration $\delta$ = 37.86 ms and gradient separation = 43.1 ms.

## 4. Results

### 4.1. Results of Synthetic Data

**On Selecting the Optimal Hypersphere Radius—**Choosing the optimal hypersphere radius $r_o$ for the HSH framework may be determined by plotting the NMSE of the signal fit versus $r_o$. Specifically, the HSH-interpolated signal evaluations for a specific hypersphere radius are merged across all five shells and then the NMSE is computed with respect to the ground truth. We seek the radius that yields the smallest NMSE. Fig. 2 shows plots of the NMSE as a function of $r_o$ at 45° crossing, in absence of noise, for different truncation orders of the HSH basis: $N = 2$ ($W = 14$), $N = 3$ ($W = 30$), and $N = 4$ ($W = 55$). A unique value of $r_o$ that minimizes the NMSE of the signal fit can be found for each truncation order $N$, and the results are summarized in Table 5.

Fig. 3 shows plots of the NMSE as a function of $r_o$ at 75° crossing, in absence of noise, and the optimal radius for each truncation order is displayed in Table 6. Going from 45° to 75° fiber crossing only slightly changes the optimal $r_o$ for $N = 2$ and $N = 3$ HSH reconstruction. The influence of crossing angle on the choice of hypersphere radius is moderately more pronounced for $N = 4$ HSH reconstruction, going from $p_o = 54$ to $p_o = 46$. However, as we will show later, using either $p_o = 54$ and $p_o = 46$ for $N = 4$ HSH reconstruction will not significantly affect the dODF reconstruction.

**HSH Signal Reconstruction—**Fig. 4 displays the HSH signal fit at 45° crossing, in absence of noise, for different truncation orders $N$ of the HSH basis. Naturally, as the truncation order increases, the quality of the signal fit improves, with the $N = 4$ HSH reconstruction fitting the signal attenuation nearly perfectly across all $b$-values. But even the $N = 2$ HSH reconstruction, which is expending only 14 coefficients, fits the signal quite well.

Fig. 5 displays the $N = 4$ HSH signal fit at 75° crossing in absence of noise using the optimal radius for both 45° and 75° crossings. The signal fit is nearly identical, and indicates that the HSH signal reconstruction is not seriously affected when using the optimal radius for 45° crossing in the 75° case.

**dODF Estimation—**Fig. 6 shows the HSH-estimated dODF at various truncation orders, BFOR-estimated dODF, and ground truth dODF for 45° crossing. Note that the $N = 2, 3,$ and 4 HSH-estimations are remarkably similar to one another, with the KLD only slightly increasing as the truncation order increases. At all three truncation orders, the HSH basis successfully captures the geometry and orientation of the dODF profile. However, the HSH basis somewhat smoothens the dODF peaks. The BFOR-estimated dODF is not as accurate as those of the HSH, with even its KLD being much higher than the $N = 2$ HSH-estimation. Both Figs. 4 and 6 suggest that only 14 HSH-coefficients (i.e. $N = 2$ HSH-estimation) are sufficient to characterize the signal attenuation and dODF.

Fig. 7 displays the $N = 4$ HSH-estimated dODF for 75° crossing using the optimal radius for both 45° and 75° crossing cases. Again, as with the signal fit, the dODF reconstructions are nearly identical, so the HSH estimation of the dODR is not seriously affected when using the optimal radius for 45° crossing in the 75° case. And similar to the dODF reconstruction at 45° crossing, the HSH basis successfully captures the geometry and orientation of the dODF profile, but again somewhat smoothens the dODF peaks.

Although the optimal radius for $N = 4$ HSH reconstruction is somewhat more influenced by fiber crossing angle than that of lower truncation orders, based on the results of both Figs. 5 and 7, we see that using the optimal radius for one fiber crossing angle will not seriously affect the results for another crossing angle. For this reason, we will henceforth employ each truncation order's optimal radius at the 45° crossing case for all subsequent analysis.

**Robustness to Noise—**Fig. 8 displays the noise simulation results on the signal fit for the HSH and BFOR bases, with the NMSE plotted against SNR for each $b$-value. There is very little disparity between the HSH and BFOR bases for the first three $b$-values. At the fourth shell for SNR= 10, the NMSE of the HSH basis is less than 5%, while that of BFOR exceeds 5%. At the outermost shell for SNR= 10, the NMSE of the HSH basis is at most 15%, while that of BFOR is more than twice that.

Table 7 displays the noise simulation results on the dODF estimation for 45° crossing, with the KLD and angular error computed across 1000 trials at SNR= 10. As the truncation order of the HSH basis decreases, both the KLD and angular error likewise decrease; the KLD and angular error of the $N = 2$ reconstructions is about one-fifth and one-half, respectively, that of the $N = 4$ reconstruction. The BFOR estimation is the most sensitive to noise, with its KLD about twice as high as the $N = 4$ HSH-estimation. BFOR's angular error is slightly lower that of the $N = 4$ HSH reconstruction.

Similarly, Table 8 displays the noise simulation results on the dODF estimation for 75° crossing, with the KLD and angular error computed across 1000 trials at SNR= 10. Again, as the truncation order of the HSH of the HSH basis decreases, both the KLD and angular error likewise decrease; the KLD and angular error of the $N = 2$ reconstructions is about one-fifth and one-half, respectively, that of the $N = 4$ reconstruction. Note that the KLD and angular errors at 75° are similar to those at 45°.

The lack of robustness of higher order HSH expansion to noise can simply be attributed to how the model fits the data. The HSH basis expansion, like any Fourier expansion, wiggles around the data in order to fit it in the least squares sense. In our situation, at higher orders, we see that the HSH expansion wiggles more than at lower orders, so it does not the fit the data as well. Equivalently, lower order HSH expansions smoothen out the noise, while higher order ones capture more noise.

Both Fig. 8 and Table 7 indicate that the HSH basis is more robust to noise than BFOR, with even the lowest order HSH estimation outperforming BFOR. The $N = 2$ HSH reconstruction is slightly more robust to noise than higher order HSH reconstructions, as assessed by the NMSE of the signal fit. But in terms of the KLD and angular error of dODF estimation, the

$N = 2$ HSH reconstruction is much more robust to noise than higher order HSH reconstructions. Most importantly, the noise simulations suggest that the 14 fitting parameters from the $N = 2$ estimation are more than adequate to accurately compute both the signal attenuation and dODF.

## 4.2. Results of In Vivo Data

**Imposing Antipodal Symmetry**—The HSH basis is not symmetric on the hypersphere (since both odd and even HSH are used), which poses a problem with regards to *in vivo* dODF reconstruction. Unlike synthetic experiments, where the *q*-space signal is guaranteed to be symmetric, the *q*-space signal acquired from *in vivo* data may not be symmetric due to noise, motion, geometric distortion, etc. Such asymmetry does not pose a problem for the BFOR basis because its inherent symmetry will impose symmetry on the *in vivo* data. However, for the HSH basis, asymmetric *in vivo* data will result in asymmetric dODF profiles. Since the *q*-space signal is theoretically a symmetric (i.e. even) function, we get around this problem by requiring that the *in vivo* data satisfies

$$E(\mathbf{q}) = E(-\mathbf{q})$$

That is, the mathematical reflection of the *q*-space coordinates (used in the acquisition) outputs the measured *in vivo* signal. Essentially, we are inflating our data not by acquiring more data, but by exploiting prior information regarding the *q*-space signal (in this case, its symmetry). Henceforth, symmetry will be imposed on all *in vivo* calculations using the HSH basis.

***In Vivo* dODF Profiles**—In Fig. 9, a $4 \times 4$ ROI was drawn on the splenium of corpus callosum. The dODF profile for each voxel in the ROI was estimated using the HSH basis at $N = 2$, 3, & 4. The dODF profiles at each truncation order have the fundamental peanut shape (i.e. mono- directional) of a single fiber. Although the $N = 4$ reconstruction is sharper, the $N = 2$ and 3 reconstructions are congruous with that of $N = 4$ in terms of overall shape and orientation of fibers, and so suggesting that 14 HSH coefficients are sufficient to characterize single fibers.

In Fig. 10, a $4 \times 4$ ROI was drawn on a region of crossing fibers. The dODF profile for each voxel in the ROI was estimated using the HSH basis at $N = 2$, 3, & 4. Fiber crossing configurations are recovered and well discriminated by each truncation order. As expected, the $N = 4$ HSH reconstruction is sharper, whereas those of $N = 2$ and 3 are more smoothened. However, congruity exists across all three reconstructions in terms of overall shape and orientation.

**Quantitative Indices**—Axial slices of *Po*, computed via HSH and BFOR bases, are shown in Fig. 11. The $N = 2$, 3, and 4 HSH-estimations of *Po* are nearly identical and they closely resemble BFOR's, exhibiting both tissue/CSF and WM/GM contrasts. The HSH *Po* maps, however, have sharper WM/GM contrast than BFOR's (compare the left and right putamen in both maps), which probably arises from the signal weighting operation. The

results suggest that 14 HSH coefficients, i.e. $N = 2$ HSH reconstruction, are adequate in estimating *Po*.

Axial slices of QIV, computed via HSH and BFOR bases, are shown in Fig. 12. The $N = 2$, 3, and 4 HSH-estimations of QIV are nearly identical and they closely resemble BFOR's, exhibiting both rich tissue/CSF and WM/GM contrasts. However, BFOR's QIV map has some voxels that blow up upon the division operation in computing QIV, which are zeroed out in Fig. 12d, but this was not the case for the HSH-estimated QIV. As with the *Po* estimation, the results indicate that 14 HSH coefficients, i.e. $N = 2$ HSH reconstruction, are adequate in estimating QIV.

## 5. Discussion

We have demonstrated that the $N = 2$ HSH reconstruction, which expends only 14 fitting parameters, is more than adequate in resolving crossing fiber configurations and estimating quantitative metrics like *Po* and QIV. The noise simulations indicate that it is more robust than higher order HSH reconstructions and BFOR.

The HSH framework, as with MAP-MRI, captures both the radial and angular contents of the *q*-space signal with a single basis function, while BFOR employs two basis functions: one radial (spherical Bessel function) and angular (spherical harmonics). BFOR's use of the spherical Bessel function to model the *q*-space signal is unrealistic because it infinitely oscillates about zero, while the *q*-space signal radially decays to zero. Table 9 compares the number of fitting parameters between BFOR, HSH, and MAP-MRI.

The HSH framework also suffers several limitations. First, the hyperspherical interpretation of *q*-space destroys, via stereographic projection, the *q*-space signal's inherent symmetry. However, this can be remedied by imposing antipodal symmetry on the *in vivo* data. Second, the complexity of fiber architecture, as reflected by the crossing angle, somewhat affects the choice of hypersphere radius, especially at higher truncation orders. However, as our synthetic results have shown, employing one crossing angle's optimal radius for some other crossing angle will not significantly affect the results.

The major drawback of the HSH framework is the difficulty in analytically estimating the EAP via Eq. 14 due to the non-volume preserving nature of stereographic projection. Although the signal basis is analytical in the HSH framework, the dODF and *q*-space metrics can not be analytically estimated. The HSH framework requires the *q*-space measurements to be regridded onto and interpolated on a Cartesian lattice, as done in DSI and HYDI, in order to estimate the dODF. And *ad hoc* correction of the *Po* and QIV maps is needed to correct for volume distortion. It should be noted, however, that such numerical computations do not significantly impede computational efficiency. BFOR's key advantage over the HSH framework is its analytical estimation of the diffusion propagator and various *q*-space metrics.

Although the encoding scheme in this study consisted of hybrid sampling along equally spaced concentric spherical shells, the HSH framework does not require such a scheme. A minimum of two diffusion weightings is required, however. Random sampling along *q*-

space or even the use of unequally spaced concentric shells is perfectly valid. This, however, leads to the important question of what is the best way to sample *N* diffusion measurements in *q*-space, which have started to be addressed (Assemlal et al., 2009b; Merlet et al., 2011; Koay et al., 2012; Caruyer et al., 2013). Although the HSH framework's efficient representation of the dODF may also make it conducive to compressed sensing (Menzel et al., 2011; Merlet and Deriche, 2013; Paquette et al., 2014), the HSH basis is global; localized functions, by virtue of possessing compact support, will have better sparsity than global bases. Future work includes optimizing the HYDI *q*-space sampling and exploring the sparsibility of the HSH basis.

The dODF profiles are not sharp enough to extract the true fiber orientation, as clearly seen in Fig. 10. Rather, the fiber orientation is given by the fiber orientation distribution function (fODF), which can be computed via spherical deconvolution of some assumed kernel (i.e. response function) from the *q*-space diffusion signal (Tournier et al., 2004; Descoteaux et al., 2009). Analytical estimation of the fODF using the HSH framework will be difficult because of the stereographic projection's volume distortion. However, similar to the dODF estimation, the fODF can be estimated numerically by evaluating the spherical deconvolution via the Richardson-Lucy algorithm (Parker et al., 2013), which will be left as future work.

## 6. Conclusion

We have introduced a new orthonormal basis to model the 3D *q*-space signal, and from which various *q*-space metrics can be computed. 4D HSH signal modeling allows for the capture of the radial and angular contents of the diffusion profile by a single basis function, and the basis' orthonormality provides robust numerical stability. Importantly, we have demonstrated the HSH basis' ability to sparsely represent the diffusion process. In fact, the second order HSH reconstruction, which expends 14 fitting parameters, can adequately resolve crossing fiber configurations and estimate *q*-space indices. Such robust performance by a sparse representation implies that the HSH framework may be better suited to sparser sampling schemes than BFOR, which will be explored in the future. Although the hyperspherical interpretation of *q*-space destroys, via stereographic projection, the signal's inherent symmetry, this can be remedied by imposing antipodal symmetry on the *in vivo* data. The major drawback of the HSH framework is the difficulty in analytically estimating the EAP.

## Acknowledgments

## References

Aganj I, Lenglet C, Sapiro G, Yacoub E, Ugurbil K, Harel N. Reconstruction of the orientation distribution function in single- and multiple-shell q-ball imaging within constant solid angle. Magn Reson Med. 2010; 64:554–566. [PubMed: 20535807]

Assaf Y, Cohen Y. Non-mono-exponential attenuation of water and n-acetyl aspartate signals due to diffusion in brain tissue. J Magn Reson. 1998; 131:69–85. [PubMed: 9533908]

Assaf Y, Mayk A, Cohen Y. Displacement imaging of spinal cord using q-space diffusion-weighted MRI. Magn Reson Med. 2000; 44:713–722. [PubMed: 11064406]

Assemlal HE, Tschumperlé D, Brun L. Efficient and robust computation of PDF features from diffusion MR signal. Med Image Anal. 2009a; 13:715–729. [PubMed: 19665917]

Assemlal HE, Tschumperlé D, Brun L. Evaluation of q-space sampling strategies for the diffusion magnetic resonance imaging. MIC-CAI. 2009b:482–489.

Bar-Shir A, Avram L, Ozarslan E, Basser PJ, Cohen Y. The effect of the diffusion time and pulse gradient duration ratio on the diffraction pattern and the structural information estimated from q-space diffusion MR. J Magn Reson. 2008; 194:230–236. [PubMed: 18667345]

Basser PJ. Relationships between diffusion tensor and q-space MRI. Magn Reson Med. 2002; 47:392–397. [PubMed: 11810685]

Basser PJ, Mattiello J, LeBihan D. MR diffusion tensor spectroscopy and imaging. Biophysical Journal. 1994; 66:259–267. [PubMed: 8130344]

Callaghan, PT. Principles of Nuclear Magnetic Resonance Microscopy. Oxford University Press; Oxford: 1991.

Canales-Rodriguez EJ, Lin CP, Iturria-Medina Y, YCH, Cho KH, Melie-Garcia L. Diffusion orientation transform revisited. NeuroImage. 2010; 49:1326–1339. [PubMed: 19815083]

Canales-Rodriguez EJ, Melie-Garcia L, Iturria-Medina Y. Mathematical description of q-space in spherical coordinates: exact q-ball imaging. Magn Reson Med. 2009; 61:1350–1367. [PubMed: 19319889]

Caruyer E, Lenglet C, Sapiro G, Deriche R. Design of multi-shell sampling schemes with uniform coverage in diffusion MRI. Mag Reson Med. 2013; 69:1534–1540.

Cheng, J.; Ghosh, A.; Deriche, R.; Jiang, T. MICCAI. Springer; Heidelberg: 2010a. Model-free, regularized, fast, and robust analytical orientation distribution function estimation; p. 648-656.

Cheng, J.; Ghosh, A.; Jiang, T.; Deriche, R. MICCAI. Springer; Heidelberg: 2010b. Model-free and analytical EAP reconstruction via spherical polar Fourier diffusion MRI; p. 590-597.

Clark CA, Le Bihan D. Water diffusion compartmentation and anisotropy at high b values in the human brain. Magn Reson Med. 2000; 44:852–859. [PubMed: 11108621]

Descoteaux M, Angelino E, Fitzgibbons S, Deriche R. Regularized, fast, and robust analytical q-ball imaging. Magn Reson Med. 2007; 58:497–510. [PubMed: 17763358]

Descoteaux M, Deriche R, Knosche TR, Anwander A. Deterministic and probabilistic tractography based on complex fibre orientation distributions. IEEE Transac Med Imaging. 2009; 28:269–286.

Descoteaux M, Deriche R, LeBihan D, Mangin JF, Poupon C. Multiple q-shell diffusion propagator imaging. Med Image Anal. 2011; 15:603–621. [PubMed: 20685153]

Domokos G. Four-dimensional symmetry. Physical Review. 1967; 159:1387–1403.

Fock V. Zur theorie des wasserstoffatoms. Z Physik. 1935; 98:145–154.

Hess CP, Mukherjee P, Han ET, Xu D, Vigneron DB. Q-ball reconstruction of multimodal fiber orientations using the spherical harmonic basis. Magn Recon Med. 2006; 56:104–117.

Hosseinbor AP, Chung MK, Wu YC, Alexander AL. Bessel Fourier orientation reconstruction (BFOR): an analytical diffusion propagator reconstruction for hybrid diffusion imaging and computation of q-space indices. Neuroimage. 2013a; 64:650–670. [PubMed: 22963853]

Hosseinbor, AP.; Chung, MK.; Wu, YC.; Alexander, AL.; Bendlin, BB. MICCAI. Springer; Heidelberg: 2013b. A 4D hyperspherical interpretation of q-space; p. 501-509.

Hosseinbor, AP.; Chung, MK.; Wu, YC.; Fleming, JO.; Field, AS.; Alexander, AL. MICCAI. Springer; Heidelberg: 2012. Extracting quantitative measures from EAP: a small clinical study using BFOR; p. 280-287.

Koay C, Ozarslan E, Johnson KM, Meyerand ME. Sparse and optimal acquisition design for diffusion MRI and beyond. Medical Physics. 2012; 39:2499–2511. [PubMed: 22559620]

Koay CG, Ozarslan E, Basser PJ. A signal transformational framework for breaking the noise floor and its applications in MRI. J Magn Reson. 2009; 197:108–119. [PubMed: 19138540]

Maier SE, Vajapeyam S, Mamata H, Westin CF, Jolesz FA, Mulkern RV. Biexponential diffusion tensor analysis of human brain diffusion data. Magn Reson Med. 2004; 51:321–330. [PubMed: 14755658]

Mair RW, Sen PN, Hurlimann MD, Patz S, Cory DG, Walsworth RL. The narrow pulse approximation and long length scale determination in xenon gas diffusion NMR studies of model porous media. J Magn Reson. 2002; 156:202–212. [PubMed: 12165255]

Menzel MI, Tan ET, Khare K, Sperl JI, King KF, Tao X, Hardy CJ, Marinelli L. Accerlerated diffusion spectrum imaging in the human brain using compressed sensing. Magn Reson Med. 2011; 66:1226–1233. [PubMed: 22012686]

Merlet S, Caruyer E, Deriche R. Impact of radial and angular sampling on multiple shells acquisition in diffusion MRI. MICCAI. 2011:113–121. [PubMed: 22003607]

Merlet S, Deriche R. Continuous diffusion signal, EAP, and ODF estimation via compressive sensing in diffusion MRI. Medical Image Analysis. 2013; 17:556–572. [PubMed: 23602920]

Michailovich O, Rathi Y, Dolui S. Spatially regularized compressed sensing for high angular resolution diffusion image. IEEE Transac Med Imaging. 2011; 30:1100–1115.

Mulkern RV, Gudbjartsson H, Westin CF, Zengingonul HP, Gartner W, RGC, Robertson R, WK, Schwartz R, Holtzman D, Jolesz FA, Maier SE. Multi-component apparent diffusion coefficients in human brain. NMR Biomed. 1999; 12:51–62. [PubMed: 10195330]

Niendorf T, Dijkhuizen RM, Norris DG, van Lookeren Campagne M, Nicolay K. Biexponential diffusion attenuation in various states of brain tissue: implications for diffusion-weighted imaging. Magn Reson Med. 1996; 36:847–857. [PubMed: 8946350]

Ozarslan E, Koay C, Shepherd TM, Blackband SJ, Basser PJ. Simple harmonic oscillator based reconstruction and estimation for three-dimensional q-space MRI. Proc Intl Soc Mag Reson Med. 2009

Ozarslan E, Koay CG, Basser PJ. Simple harmonic oscillator based estimation and reconstruction for one-dimensional q-space MR. Proc Intl Soc Mag Reson Med. 2008

Ozarslan E, Koay CG, Shepherd TM, Komlosh ME, Irfanoglu MO, Pierpaoli C, Basser PJ. Mean apparent propagator (MAP) MRI: a novel diffusion imaging method for mapping tissue microstructure. NeuroImage. 2013; 78:16–32. [PubMed: 23587694]

Paquette M, Merlet S, Gilbert G, Deriche R, Descoteaux M. Comparison of sampling strategies and sparsifying transforms to improve compressed sensing diffusion spectrum imaging. Magn Reson Med. 2014

Parker GD, Marshall D, Rosin PL, Drage N, Richmond S, Jones DK. A pitfall in the reconstruction of fibre ODFs using spherical deconvolution of diffusion MRI data. NeuroImage. 2013; 65:433–448. [PubMed: 23085109]

Rathi, Y.; Michailovic, O.; Setsompop, K.; Bouix, S.; Shenton, ME.; Westin, CF. MICCAI. Springer; Heidelberg: 2011. Sparse multi-shell diffusion imaging; p. 58-65.

Schrödinger E. Quantisierung als eigenwertproblem. Annalen der Physik. 1926; 385:437–490.

Stejskal E, Tanner J. Spin diffusion measurements: spin echoes in the presence of a time-dependent field gradient. J Chem Phys. 1965; 42:288–292.

Tournier JD, Calamante F, Gadian DG, Connelly A. Direct estimation of the fiber orientation density function from diffusion-weighted MRI data using spherical deconvolution. NeuroImage. 2004; 23:1176–1185. [PubMed: 15528117]

Tristan-Vega A, Westin CF, Aja-Fernandez S. Estimation of fiber orientation probability density functions in high angular resolution diffusion imaging. NeuroImage. 2009; 47:638–650. [PubMed: 19393321]

Tuch DS. Q-ball imaging. Magn Reson Med. 2004; 52:1358–1372. [PubMed: 15562495]

Tuch DS, Reese TG, Wiegell MR, Makris N, Belliveau JW, Weeden VJ. High angular resolution diffusion imaging reveals intravoxel white matter fiber heterogeneity. Magn Reson Med. 2002; 48:577–582. [PubMed: 12353272]

Weeden VJ, Hagmann P, Tseng WYI, Reese TG, Weisskoff RM. Mapping complex tissue architecture with diffusion spectrum magnetic resonance imaging. Magn Reson Med. 2005; 54:1377–1386. [PubMed: 16247738]

Wong STS, Roos MS. A strategy for sampling on a sphere applied to 3D selective RF pulse design. Magn Reson Med. 1994; 32:778–784. [PubMed: 7869901]

Wu YC, Alexander AL. Hybrid diffusion imaging. NeuroImage. 2007; 36:617–629. [PubMed: 17481920]

Wu YC, Field AS, Alexander AL. Computation of diffusion function measures in q-space using magnetic resonance hybrid diffusion imaging. IEEE Transac Med Imaging. 2008; 27:858–865.

## Appendix A. 1D-to-2D Analogue of Eq. (14)

A better understanding of the integral transform described by Eq. (14) can be obtained by considering the simpler 1D-to-2D scenario. Consider two infinite 1D lines, one defined by the variable $x$ and the other by $k$. We assume the integral transform mapping from $x$-space to $k$-space is the Fourier transform; in other words,

$$F(k) = \int_{-\infty}^{\infty} f(x) e^{-2\pi i k x} dx. \quad \text{(Appendix A.1)}$$

Now lets stereographically project each line onto a circle of radius $r_o$. Stereographic projection establishes a one-to-one correspondence between the 1D plane and circle.

Let's first consider 1D $x$-space. According to stereographic projection, any point $x$ on the line maps to a unique point $(u, v) = (r_o \cos\theta, r_o \sin\theta)$ along the circle, where $\theta \in [0, 2\pi]$. The exact relationship between $x$ and $(u, v)$ given by

$$\begin{aligned} u &= \frac{2r_o^2 x}{x^2 + r_o^2} = r_o \cos\theta \\ v &= \frac{r_o(x^2 - r_o^2)}{x^2 + r_o^2} = r_o \sin\theta \end{aligned} \quad \text{(Appendix A.2)}$$

Using Eq. (Appendix A.2), we can deduce that

$$x = r_o \sqrt{\frac{1 + \sin\theta}{1 - \sin\theta}} \quad \text{(Appendix A.3)}$$

and

$$\frac{d\theta}{dx} = \frac{2r_o^2}{x^2 + r_o^2} = \frac{1 - \sin\theta}{r_o} \quad \text{(Appendix A.4)}$$

Similarly, we project 1D $k$-space onto a circle of radius $r_o$. According to stereographic projection, the relationship between a point $k$ on the line and the point $(u', v') = (r_o \cos\theta', r_o \sin\theta')$ along the circle is

$$\begin{aligned} u' &= \frac{2r_o^2 k}{k^2 + r_o^2} = r_o \cos\theta' \\ v' &= \frac{r_o(k^2 - r_o^2)}{k^2 + r_o^2} = r_o \sin\theta' \end{aligned} \quad \text{(Appendix A.5)}$$

Using Eq. (Appendix A.5), we can deduce that

$$k = r_o \sqrt{\frac{1 + \sin\theta'}{1 - \sin\theta'}} \quad \text{(Appendix A.6)}$$

The Fourier relationship between 1D $x$-space and $k$-space, as described by Eq. (Appendix A.1), does not hold true on the circle. The question, then, is what integral transform maps from the circle associated with $x$-space to the circle associated with $k$-space? We now proceed to derive this integral transform.

Taking the product of Eqs. (Appendix A.3) and (Appendix A.6) gives

$$kx = r_o^2 \sqrt{\frac{(1 + \sin\theta)(1 + \sin\theta')}{(1 - \sin\theta)(1 - \sin\theta')}} \quad \text{(Appendix A.7)}$$

Substituting Eqs. (Appendix A.4) and (Appendix A.7) into Eq. (Appendix A.1) gives

$$F(\theta') = r_o \int_0^{2\pi} \frac{f(\theta) e^{-2\pi i r_o^2 \Gamma(\theta, \theta')}}{1 - \sin\theta} d\theta, \quad \text{(Appendix A.8)}$$

where $\Gamma(\theta, \theta') \equiv \sqrt{\frac{(1 + \sin\theta)(1 + \sin\theta')}{(1 - \sin\theta)(1 - \sin\theta')}}$. Eq. (Appendix A.8) describes the relationship between any two functions individually existing on a circle, given that the two are Fourier transform pairs on the 1D plane.

**Research Highlights**

- Derive a 4D hyperspherical harmonic-based framework to estimate the 3D q-space signal and diffusion orientation distribution function.

- Estimate rotationally invariant *q*-space indices using our framework, like *Po* and QIV.

- Validate our framework using HYDI-acquired datasets, both synthetic and *in vivo*.

- Compare our framework to existing analytical methods, specifically BFOR.

- Derive a novel integral transform.
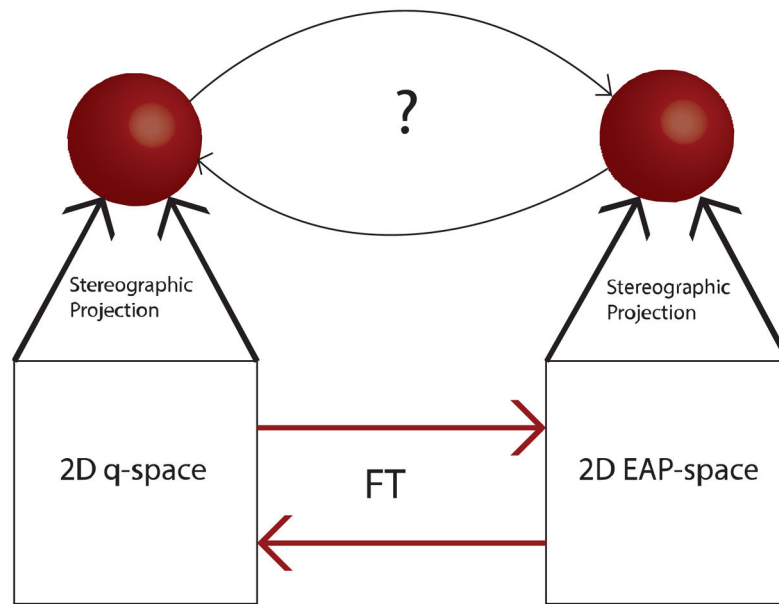
**Figure 1.**
*Q*-space and EAP-space, which are FT pair, are each stereographically projected onto a sphere. As a result, the diffusion signal and EAP each exist on a sphere, and the question then is finding the integral transform that maps from the signal-sphere
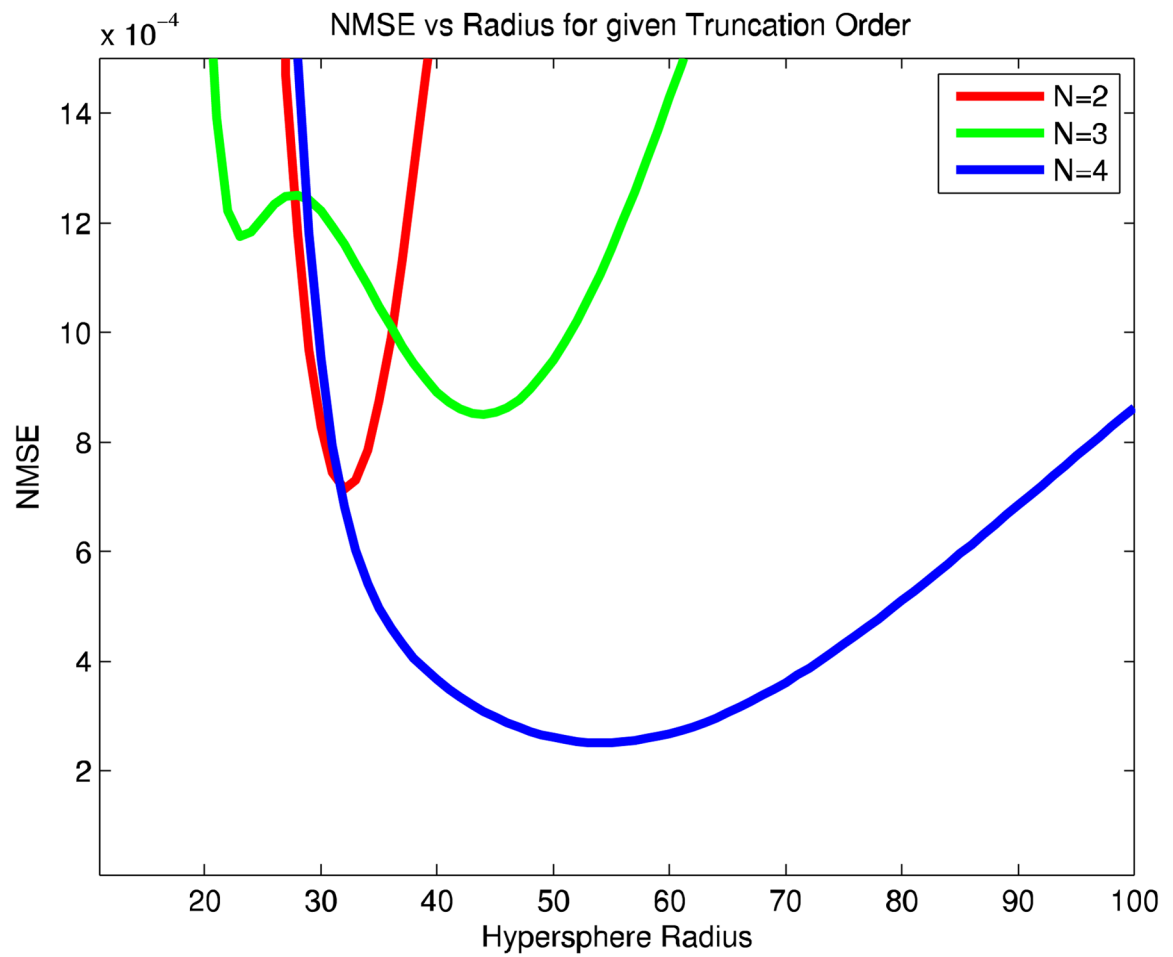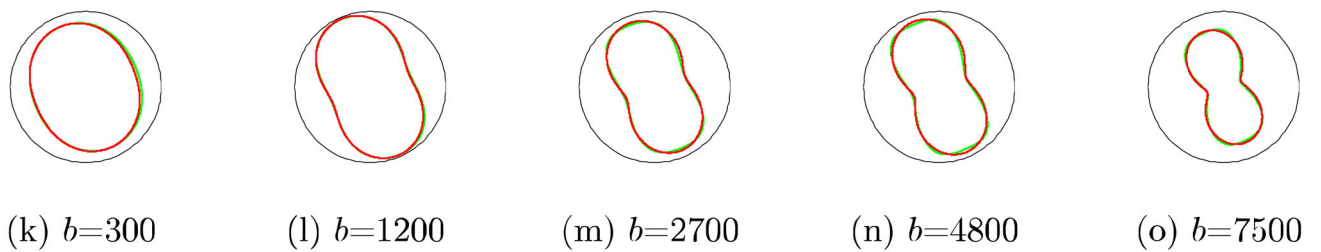
**Figure 2. 45° Fiber Crossing**
The normalized mean squared error (NMSE) of the signal fit as a function of hypersphere radius for different truncation orders *N* of the 4D HSH basis.
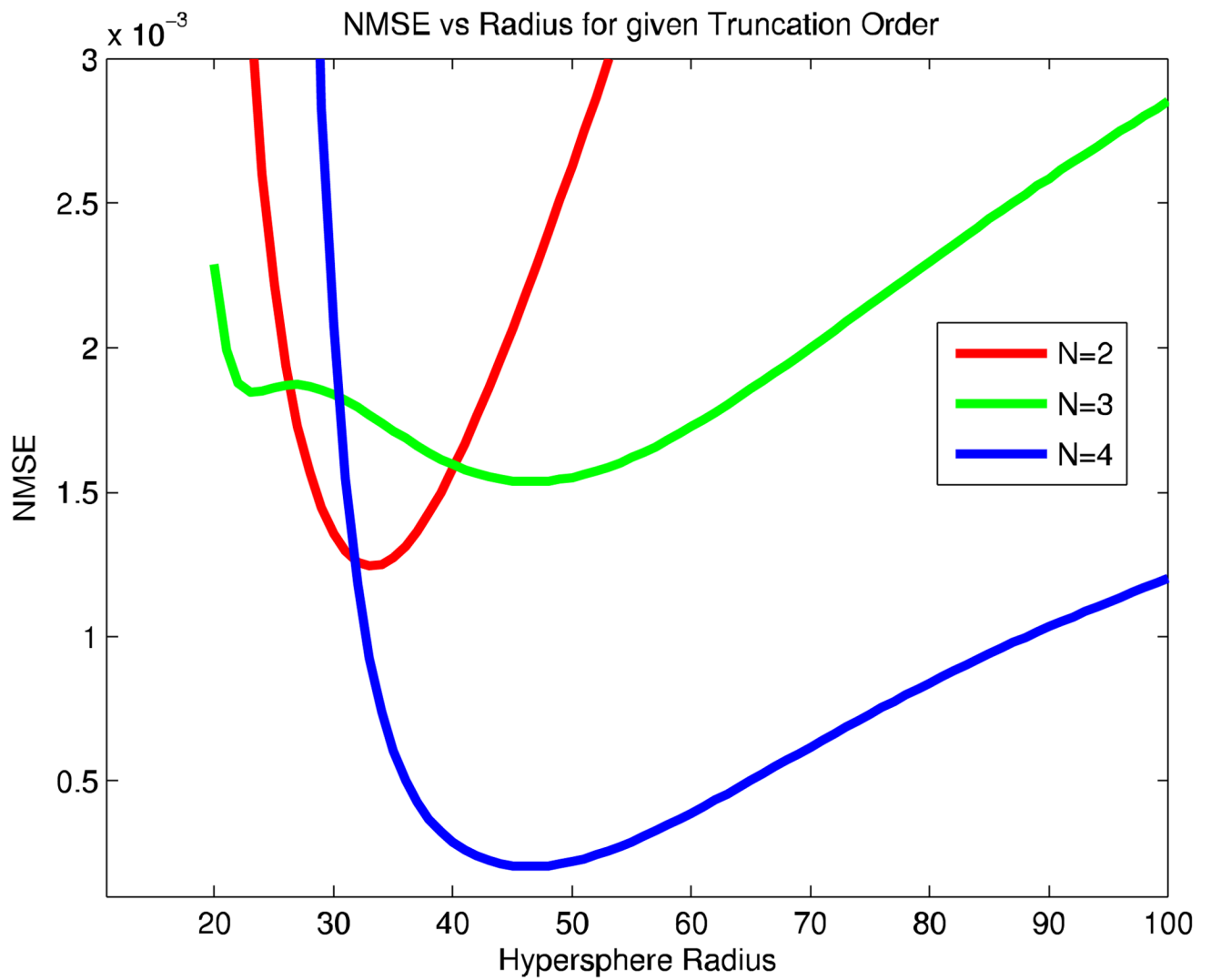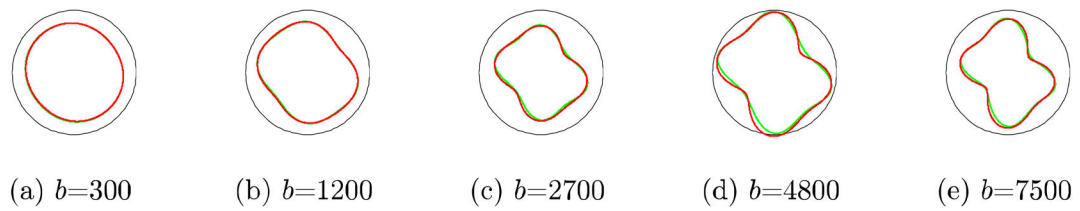
**Figure 3. 75° Fiber Crossing**
The normalized mean squared error (NMSE) of the signal fit as a function of hypersphere radius for different truncation orders *N* of the 4D HSH basis.

(a) $b$=300  (b) $b$=1200  (c) $b$=2700  (d) $b$=4800  (e) $b$=7500

$N = 2$ **HSH Signal Fit**



(f) $b$=300  (g) $b$=1200  (h) $b$=2700  (i) $b$=4800  (j) $b$=7500

$N = 3$ **HSH Signal Fit**



(k) $b$=300  (l) $b$=1200  (m) $b$=2700  (n) $b$=4800  (o) $b$=7500
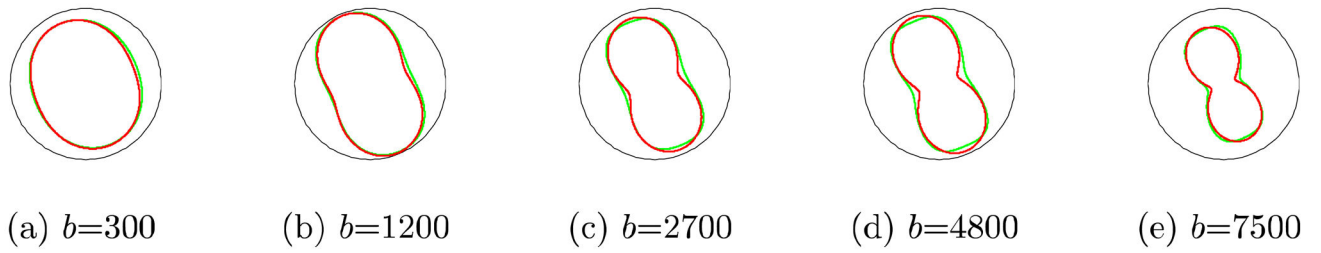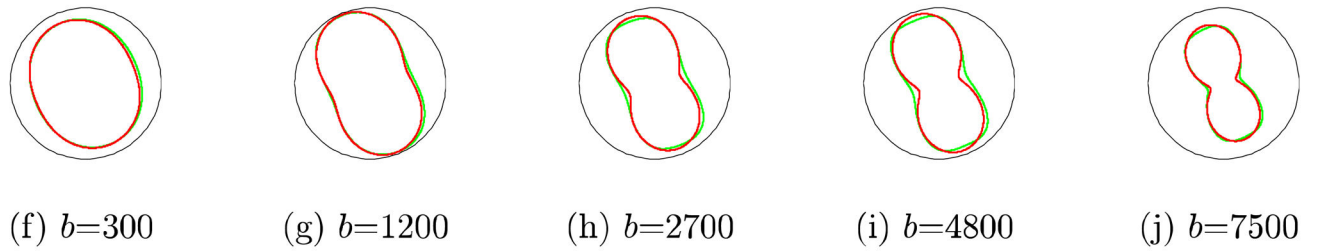
$N = 4$ **HSH Signal Fit**

**Figure 4. Signal Fit for 45° Crossing**

The ground truth diffusion signal (green) and reconstructed signal (red) using HSH basis when noise was absent. Two equally weighted WM fibers were simulated crossing at 45°. Measurements from all 5 shells were used.

(a) $b{=}300$ (b) $b{=}1200$ (c) $b{=}2700$ (d) $b{=}4800$ (e) $b{=}7500$

$N = 4$ **HSH Signal Fit at** $r_o = 46$



(f) $b{=}300$ (g) $b{=}1200$ (h) $b{=}2700$ (i) $b{=}4800$ (j) $b{=}7500$
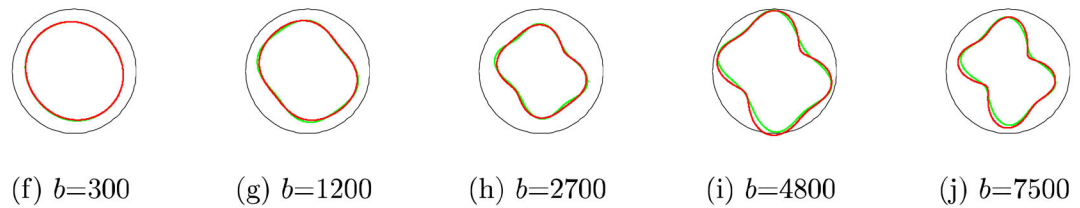
$N = 4$ **HSH Signal Fit at** $r_o = 54$

**Figure 5. Signal Fit for 75° Crossing**

The ground truth diffusion signal (green) and reconstructed signal (red) using $N = 4$ HSH basis when noise was absent. Two equally weighted WM fibers were simulated crossing at 75°. Both the optimal radius for 45° ($r_o = 54$) and 75° ($r_o = 46$) crossings are employed for $N = 4$ reconstruction. We see that the overall signal reconstruction is not seriously affected when using the optimal radius for 45° crossing in the 75° case.
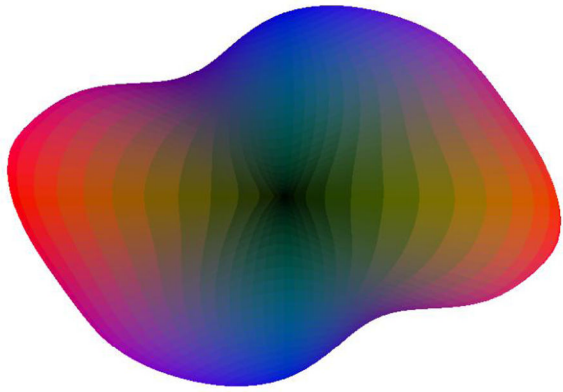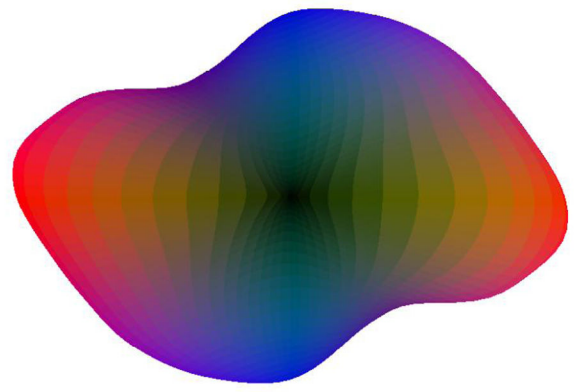
(a) HSH $N = 2$ (KLD= 0.0402)

(b) HSH $N = 3$ (KLD=0.0351)

(c) HSH $N = 4$ (KLD=0.0208)

(d) BFOR (KLD=0.147)
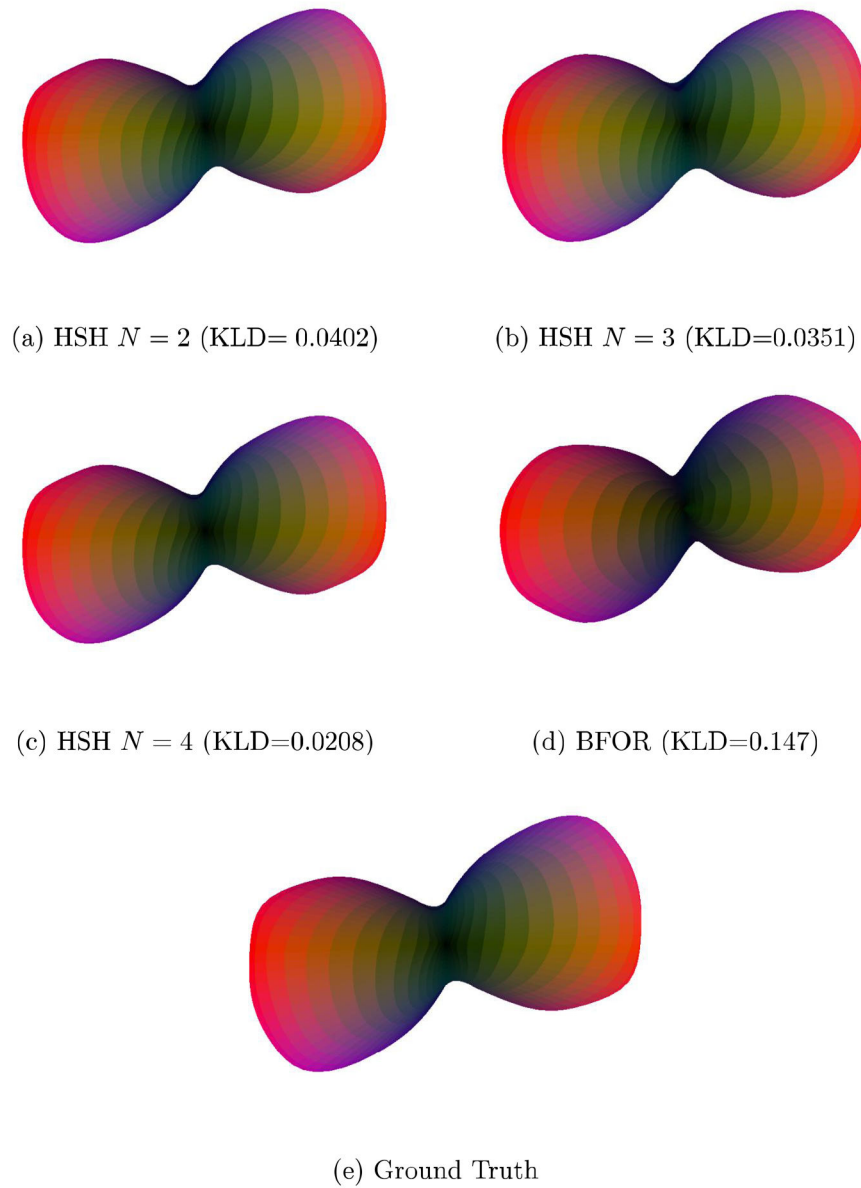
(e) Ground Truth

**Figure 6. dODF Fit for 45° Crossing**
The HSH-estimated, BFOR-estimated, and ground truth dODF's in absence of noise for two equally weighted fibers crossing at 45°. The dODF is normalized to [0 1], and the KLD with respect to the ground truth is listed for both HSH and BFOR bases.

(a) HSH $N = 4$ and $r_o = 46$                                                (b) HSH $N = 4$ and $r_o = 54$
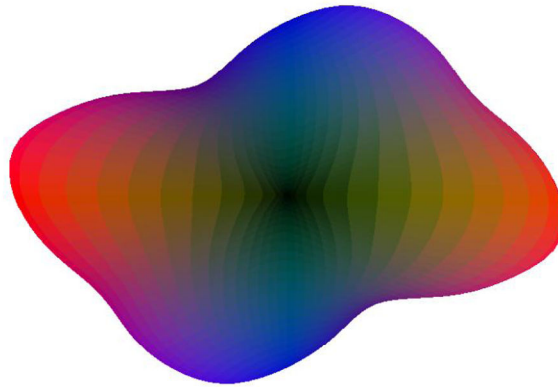
(c) Ground Truth

**Figure 7. dODF fit for 75° Crossing**
The HSH-estimated and ground truth dODF's in absence of noise for two equally weighted fibers crossing at 75°. The dODF is normalized to [0 1]. Both the optimal radius for 45° ($r_o$ = 54) and 75° ($r_o$ = 46) crossings are employed for $N = 4$ reconstruction. We see that the overall dODF reconstruction is not seriously affected when using the optimal radius for 45° crossing in the 75° case.

(a) HSH $N = 2$

(b) HSH $N = 3$

(c) HSH $N = 4$
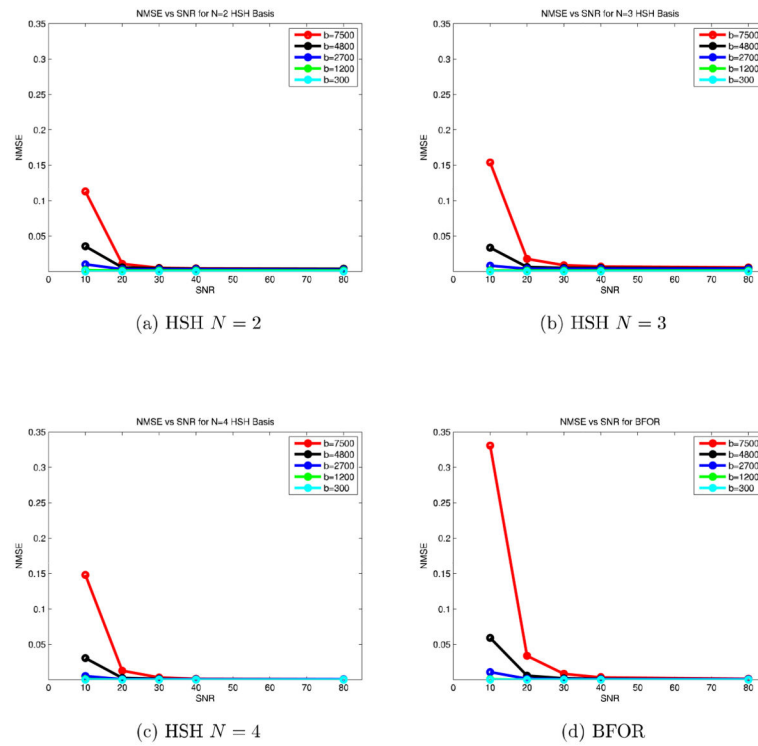
(d) BFOR

**Figure 8.**
The normalized mean squared error (NMSE) of the HSH signal fit for different truncation orders $N$ and BFOR signal fit for each $b$-value plotted against SNR. 1000 Rician noise trials were simulated for each SNR level for two equally weighted fibers crossing at 45°.
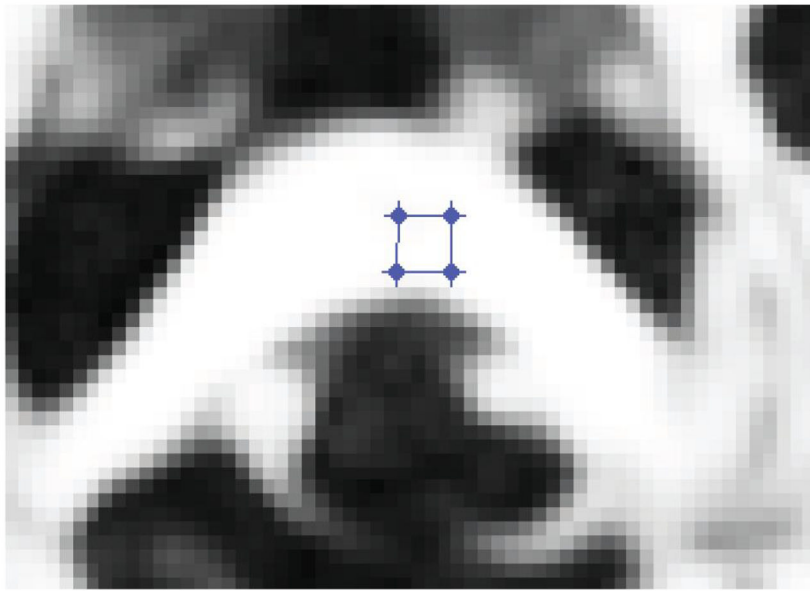
(a) GFA(10)
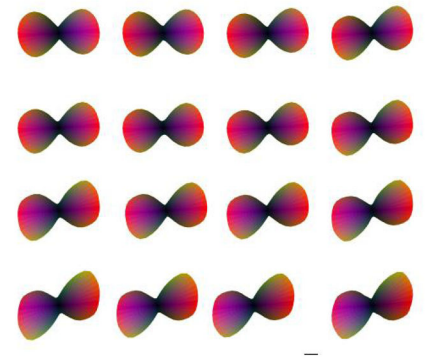
(b) $N = 2$
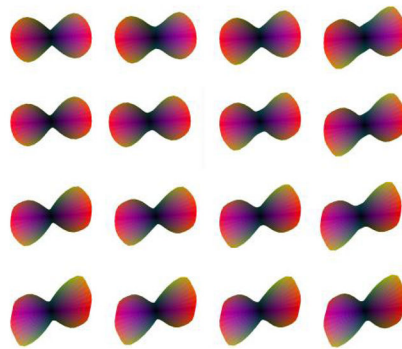
(c) $N = 3$
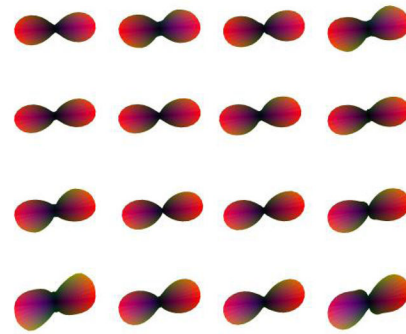
(d) $N = 4$

**Figure 9.**
Axial slice of GFA(10) map of adult human brain, where a $4 \times 4$ ROI is drawn on splenium of corpus callosum. Plotted are the HSH dODF profiles at $N =$ 2, 3, & 4 overlaid onto ROI.

(a) GFA(10)
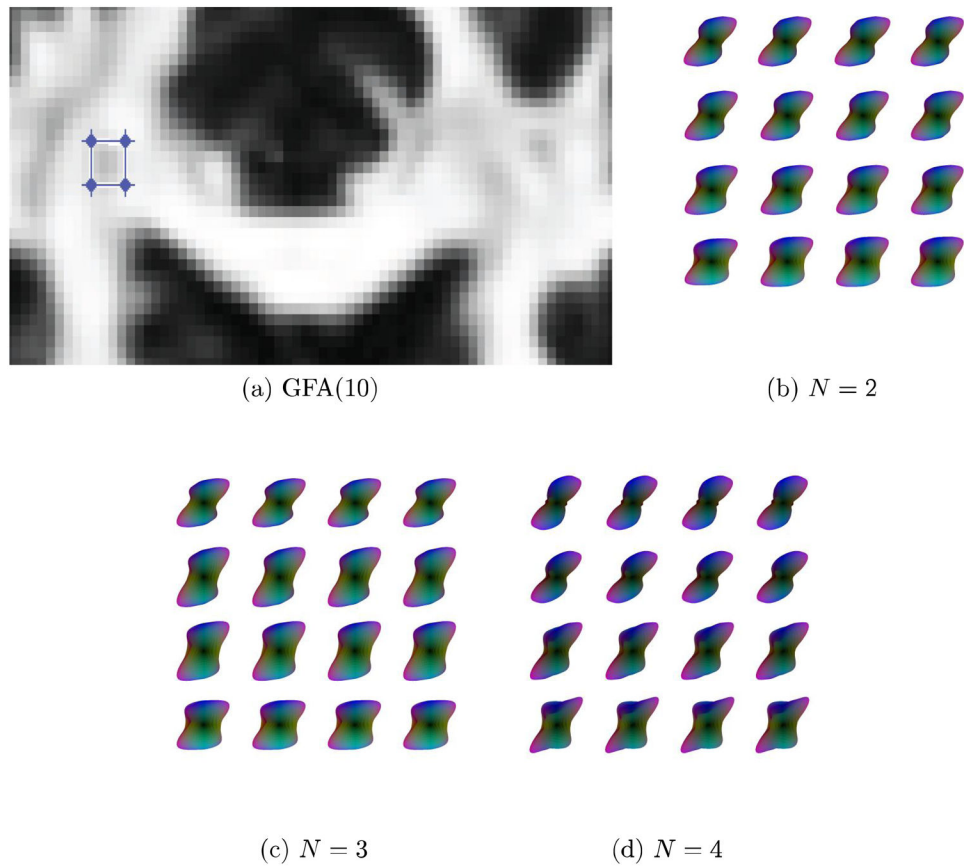
(b) $N = 2$

(c) $N = 3$

(d) $N = 4$

**Figure 10.**
Axial slice of GFA(10) map of adult human brain, where a $4 \times 4$ ROI is drawn on a region of crossing fibers. The genu of the corpus callosum is in the background. Plotted are the HSH dODF profiles at $N = 2$, 3, & 4 overlaid onto ROI.

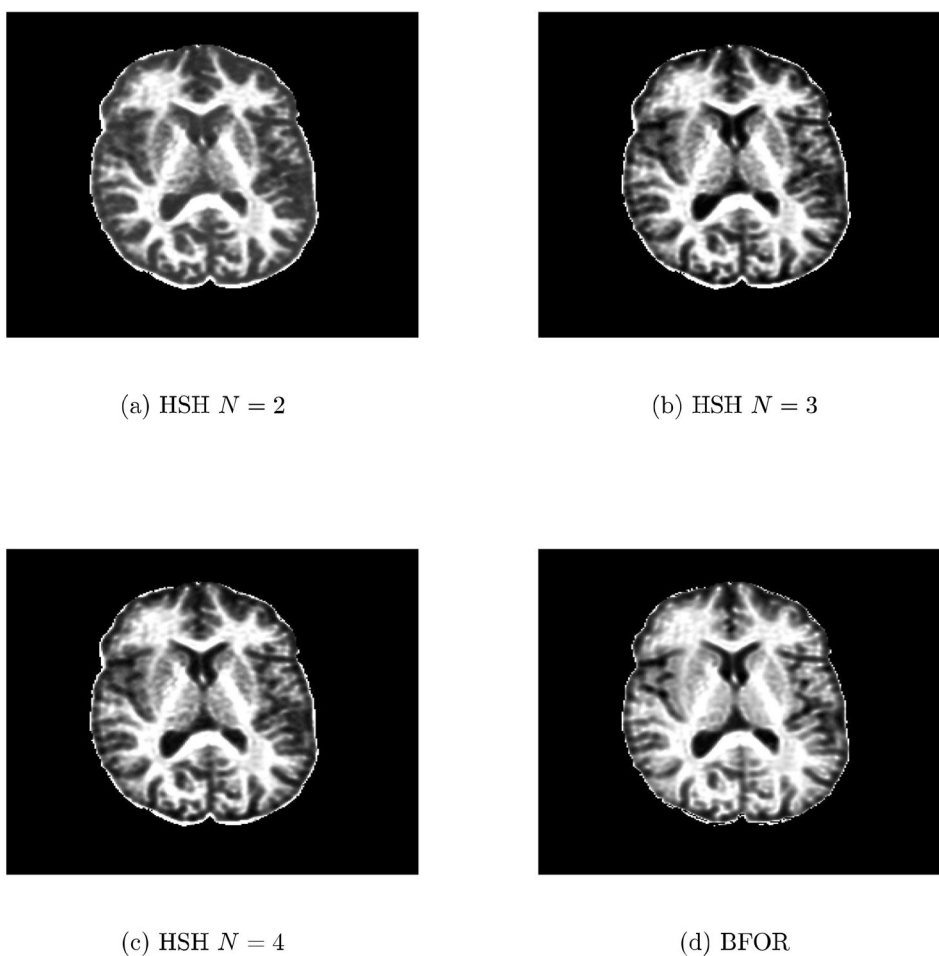(a) HSH $N = 2$



(b) HSH $N = 3$



(c) HSH $N = 4$



(d) BFOR

**Figure 11.**
Axial slices of *Po* computed via HSH and BFOR bases for a healthy, adult human. Note that antipodal symmetry was imposed on *in vivo* data in the computation of *Po*.

(a) HSH $N = 2$



(b) HSH $N = 3$
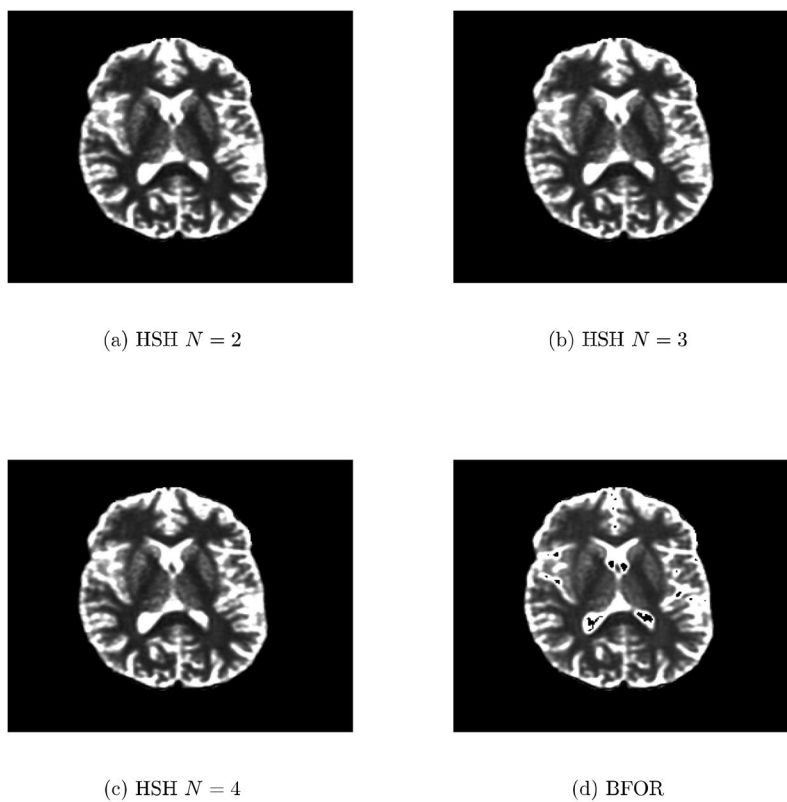


(c) HSH $N = 4$



(d) BFOR

**Figure 12.**
Axial slices of QIV computed via HSH and BFOR bases for a healthy, adult human. Note that antipodal symmetry was imposed on *in vivo* data in the computation of QIV.

**Table 1**

Summary of Non-Parametric EAP Methods

| Method | Interpretation of $q$-Space |
|---|---|
| DPI | $Q$-space signal satisfies Laplace's equation |
| SHORE | $Q$-space signal behaves like an isotropic (quantum mechanical) simple harmonic oscillator |
| SPFI | $Q$-space signal basis is a modified version of SHORE |
| MAP MRI | $Q$-space signal behaves like an anisotropic (quantum mechanical) simple harmonic oscillator |
| BFOR | $Q$-space signal satisfies the heat equation |
| SMDI | $Q$-space signal behaves like spherical ridgelets |

**Table 2**

List of a Few HSH

$$Z_{00}^0(\beta,\theta,\phi) = \frac{1}{\pi\sqrt{2}} \qquad Z_{10}^0(\beta,\theta,\phi) = \frac{\sqrt{2}}{\pi}\cos\beta$$

$$Z_{11}^{-1}(\beta,\theta,\phi) = \frac{-\sqrt{2}}{\pi}\sin\beta\sin\theta\sin\phi \qquad Z_{11}^0(\beta,\theta,\phi) = \frac{\sqrt{2}}{\pi}\sin\beta\cos\theta$$

$$Z_{11}^1(\beta,\theta,\phi) = \frac{-\sqrt{2}}{\pi}\sin\beta\sin\theta\cos\phi \qquad Z_{20}^0(\beta,\theta,\phi) = \frac{1}{\pi\sqrt{2}}(3-4\sin^2\beta)$$

$$Z_{21}^{-1}(\beta,\theta,\phi) = \frac{-\sqrt{3}}{\pi}\sin2\beta\sin\theta\sin\phi \qquad Z_{21}^0(\beta,\theta,\phi) = \frac{\sqrt{3}}{\pi}\sin2\beta\cos\theta$$

**Table 3**

HYDI Encoding Scheme

| Shell | Ne | $q$ (mm$^{-1}$) | $q$ (mm$^{-1}$) | $b$ (s/mm$^2$) |
|---|---|---|---|---|
| | 7 | 0 | | 0 |
| 1st | 6 | 15.79 | 15.79 | 300 |
| 2nd | 21 | 31.58 | 15.79 | 1200 |
| 3rd | 24 | 47.37 | 15.79 | 2700 |
| 4th | 24 | 63.16 | 15.79 | 4800 |
| 5th | 50 | 78.95 | 15.79 | 7500 |
| | Total=132 | $q_{max}$=78.95 | Mean=15.79 | $b_{max}$=7500 |

**Table 4**

Fast/Slow Diffusion ADCs & Component Size Fractions (from (Maier et al., 2004))

| Region of Interest | Corpus Callosum | Internal Capsule |
|---|---|---|
| $ADC_f$ ($\mu m^2$/ms) | 1.176 | 1.201 |
| $ADC_s$ ($\mu m^2$/ms) | 0.195 | 0.176 |
| $f_f$ | 0.699 | 0.643 |
| $f_s$ | 0.301 | 0.357 |

**Table 5**

Optimal Radius for a Given Truncation Order at 45° Crossing

| $N$ | $W$ | Optimal $r_o$ (mm$^{-1}$) | NMSE |
|---|---|---|---|
| 2 | 14 | 32 | 7.15$e$-4 |
| 3 | 30 | 44 | 8.50$e$-4 |
| 4 | 55 | 54 | 2.51$e$-4 |

**Table 6**

Optimal Radius for a Given Truncation Order at 75° Crossing

| N | W | Optimal $r_o$ (mm$^{-1}$) | NMSE |
|---|---|---|---|
| 2 | 14 | 33 | 1.25$e$-3 |
| 3 | 30 | 46 | 1.54$e$-3 |
| 4 | 55 | 46 | 2.04$e$-4 |

**Table 7**

KLD & Angular Error of dODF Estimations at SNR= 10 for 45° Crossing

| Method | KLD | Angular Error |
|---|---|---|
| HSH $N = 2$ | $0.100 \pm 0.0247$ | $7.85° \pm 4.12°$ |
| HSH $N = 3$ | $0.209 \pm 0.0540$ | $12.3° \pm 5.30°$ |
| HSH $N = 4$ | $0.528 \pm 0.109$ | $16.8° \pm 5.55°$ |
| BFOR | $1.02 \pm 0.246$ | $14.9° \pm 4.78°$ |

**Table 8**

KLD & Angular Error of dODF Estimations at SNR= 10 for 75° Crossing

| Method | KLD | Angular Error |
|---|---|---|
| HSH $N = 2$ | $0.109 \pm 0.0242$ | $7.89° \pm 4.09°$ |
| HSH $N = 3$ | $0.210 \pm 0.0526$ | $12.3° \pm 5.21°$ |
| HSH $N = 4$ | $0.472 \pm 0.108$ | $16.1° \pm 5.52°$ |

**Table 9**

Number of Fitting Parameters for Different Methods

| Method | $W$ |
|---|---|
| BFOR/SHORE | $N_{radial}(N_{angular} + 1)(N_{angular} + 2)$ |
| HSH | $(N + 1)(N + 2)(2N + 3)/6$ |
| MAP-MRI | $(N + 2)(N + 4)(2N + 3)/24$ |